Cold plasma modes in the chiral Maxwell-Carroll-Field-Jackiw electrodynamics

Filipe S. Ribeiro,[1,*] Pedro D. S. Silva,[1,†] and Manoel M. Ferreira, Jr.[2,‡]

[1]*Programa de Pós-graduação em Física, Universidade Federal do Maranhão, Campus Universitário do Bacanga, São Luís, Maranhão 65080-805, Brazil*

[2]*Departamento de Física, Universidade Federal do Maranhão, Campus Universitário do Bacanga, São Luís, Maranhão 65080-805, Brazil*

(Received 25 December 2022; accepted 21 April 2023; published 23 May 2023)

In this work, we study the propagation and absorption of plasma waves in the chiral Maxwell-Carroll-Field-Jackiw (MCFJ) electrodynamics. The Maxwell equations are rewritten for a cold, uniform, and collisionless fluid plasma model, allowing us to determine the new refractive indices and propagating modes. The cases of propagation parallel and orthogonal to the magnetic field are examined considering a purely timelike CFJ background that plays the role of the magnetic conductivity chiral parameter. The collective electromagnetic modes are associated with four distinct refractive indices associated with right-circularly polarized and left-circularly polarized waves. For each index, the propagation and absorption zones are illustrated for some specific parameter values. In low-frequency regime, we have obtained modified helicons with right- and left-circularly polarizations. The optical behavior is investigated by means of the rotatory power (RP) and dichroism coefficient. The existence of a negative refraction zone enhances the rotatory power. It is also observed RP sign reversal, a feature of rotating plasmas.

DOI: 10.1103/PhysRevD.107.096018

I. INTRODUCTION

The study of electromagnetic (EM) waves propagation [1,2] in cold magnetized plasma is based on magneto-ionic theory [3–9], developed by E. Appleton [10] and D. Hartree [11] between 1929 and 1932 to describe the radio waves propagation in the ionosphere, in the context of the usual electrodynamics [12]. EM waves in plasmas have been studied in other scenarios recently, as in logarithmic nonlinear electrodynamics [13].

The chiral magnetic effect (CME) is the macroscopic generation of an electric current in the presence of a magnetic field, stemming from an asymmetry between the number density of left- and right-handed chiral fermions [14–18]. It has been extensively investigated in several distinct contexts, such as quark-gluon plasmas [19–21], cosmology [22], neutron stars [23,24], and electroweak interactions [25]. The CME plays a very relevant role in Weyl semimetals, where it is usually connected to the chiral anomaly associated with Weyl nodal points [26], the absence of the Weyl nodes [27], anisotropic effects stemming from tilted Weyl cones [28], the CME and anomalous transport in Weyl semimetals [29], quantum oscillations arising from the CME [30], computation of the electromagnetic fields produced by an electric charge near a topological Weyl semimetal with two Weyl nodes [31], renormalization evaluations for Weyl semimetals and Dirac materials [32], and solutions of axion electrodynamics [33].

The CME current can be classically described by the axion Lagrangian [33–39],

$$\mathcal{L} = -\frac{1}{4}F^{\mu\nu}F_{\mu\nu} + \theta(\mathbf{E}\cdot\mathbf{B}), \tag{1}$$

where θ is the axion field. In this context, the Maxwell equations are

$$\nabla\cdot\mathbf{E} = \rho - \nabla\theta\cdot\mathbf{B}, \tag{2}$$

$$\nabla\times\mathbf{B} - \partial_t\mathbf{E} = \mathbf{j} + (\partial_t\theta)\mathbf{B} + \nabla\theta\times\mathbf{E}, \tag{3}$$

where the terms involving θ derivatives find association with condensed matter effects [39]. Indeed, $\nabla\theta\cdot\mathbf{B}$ represents an anomalous charge density, while $\nabla\theta\times\mathbf{B}$ appears in the anomalous Hall effect, and $(\partial_t\theta)\mathbf{B}$ plays the role of the chiral magnetic current. When we address a cold axion dark matter, the associated de Broglie wavelength is large enough to assure the inexistence of variation of the axion field in the typical dimension of experimental devices. In this case, the axion field is supposed to not depend on the space coordinates, $\nabla\theta = \mathbf{0}$, so that the Maxwell equations (2) and (3) read

*filipe.ribeiro@discente.ufma.br, filipe99ribeiro@hotmail.com
†pedro.dss@discente.ufma.br, pdiego.10@hotmail.com
‡manojr.ufma@gmail.com, manoel.messias@ufma.br

$$\nabla \cdot \mathbf{E} = \rho, \qquad \nabla \times \mathbf{B} - \partial_t \mathbf{E} = \mathbf{j} + (\partial_t \theta)\mathbf{B}, \tag{4}$$

where $(\partial_t \theta)\mathbf{B}$, the chiral magnetic current, may also be addressed as a term of Maxwell-Carroll-Field-Jackiw (MCFJ) theory. A classical electrodynamics scenario endowed with a chiral magnetic current has been investigated considering symmetric and antisymmetric conductivity [40]. The latter case has also been addressed in Ref. [41].

The MCFJ model [42] is the CPT-odd part of the $U(1)$ gauge sector of the Standard Model Extension (SME) [43]. It is described by the Lagrangian density

$$\mathcal{L} = -\frac{1}{4}F^{\mu\nu}F_{\mu\nu} - \frac{1}{4}\epsilon^{\mu\nu\alpha\beta}(k_{AF})_\mu A_\nu F_{\alpha\beta} - A_\mu J^\mu, \tag{5}$$

with $(k_{AF})_\mu$ being the 4-vector background which controls the Lorentz violation. This theory has been investigated in multiple respects [44], encompassing radiative evaluations [45,46], topological defects solutions [47], supersymmetric generalizations [48], classical solutions, quantum aspects and unitarity analysis [49]. It may also be connected with the CME in the sense that it provides a modified Ampère's law,

$$\nabla \times \mathbf{B} - \frac{\partial \mathbf{E}}{\partial t} = \mathbf{J} + k_{AF}^0 \mathbf{B} + \mathbf{k}_{AF} \times \mathbf{E}, \tag{6}$$

containing the magnetic current, $\mathbf{J}_B = k_{AF}^0 \mathbf{B}$, with the component k_{AF}^0 playing the role of the magnetic conductivity.

The SME photon sector is also composed of a CPT-even term constituted of a rank 4 Lorentz-violating tensor [50], whose components may be properly parametrized in terms of dimensionless 3×3 matrices, κ_{DE}, κ_{DB}, κ_{HE}, and κ_{HB}, which allow to write generalized constitutive relations between the fields $(\mathbf{D}, \mathbf{E})$ and $(\mathbf{H}, \mathbf{B})$,

$$\begin{pmatrix} \mathbf{D} \\ \mathbf{H} \end{pmatrix} = \begin{pmatrix} \epsilon \mathbb{1} + \kappa_{DE} & \kappa_{DB} \\ \kappa_{HE} & \mu^{-1}\mathbb{1} + \kappa_{HB} \end{pmatrix} \begin{pmatrix} \mathbf{E} \\ \mathbf{B} \end{pmatrix}, \tag{7}$$

similar to the ones that hold in continuous medium electrodynamics, see Eqs. (8a) and (8b). Here, $\mathbf{D}$ is the electric displacement, while $\mathbf{H}$ is the magnetic field. This CPT-even electrodynamics was investigated in several contexts, involving consistency aspects [51], finite temperature and boundary effects [52]. Lorentz-violating electrodynamics in continuous matter [53,54] has been a topic of interest in the latest years due to its potential to describe interesting effects of the phenomenology of new materials, such as Weyl semimetals [55]. A classical field theory description of wave propagation, refractive indices, and optical effects in a continuous medium described by the MCFJ electrodynamics (with usual constitutive relations), including its Lorentz-violating higher-order derivative version [56], was discussed in Ref. [57].

Chiral media are endowed with parity violation [58–61], being described by parity-odd models, as bi-isotropic [62] and bi-anisotropic electrodynamics [63–68], whose constitutive relations read

$$\mathbf{D} = \hat{\epsilon}\mathbf{E} + \hat{\alpha}\mathbf{B}, \tag{8a}$$

$$\mathbf{H} = \hat{\beta}\mathbf{E} + \hat{\zeta}\mathbf{B}, \tag{8b}$$

and $\hat{\epsilon} = [\epsilon_{ij}]$, $\hat{\alpha} = [\alpha_{ij}]$, $\hat{\beta} = [\beta_{ij}]$, and $\hat{\zeta} = [\zeta_{ij}]$ represent, in principle, 3×3 complex matrices. The bi-isotropic relations involve the diagonal isotropic tensors, $\epsilon_{ij} = \epsilon\delta_{ij}$, $\alpha_{ij} = \alpha\delta_{ij}$, $\beta_{ij} = \beta\delta_{ij}$. In chiral scenarios, left-circularly polarized (LCP) and right-circularly polarized (RCP) waves travel at distinct phase velocities, implying birefringence and optical rotation [69]. This phenomenon stems from the natural optical activity of the medium or can be induced by the action of external fields (e.g., Faraday effect [70–72]), and it is measured in terms of the rotation angle per unit length or rotatory power (RP) [73]. Magneto-optical effects are used to investigate features of new materials, such as topological insulators [74–80] and graphene compounds [81].

The RP is a probe to examine the optical behavior of several distinct systems, for instance, crystals [82,83], organic compounds [58,84], graphene phenomena at terahertz band [85], and gas of fast-spinning molecules [86]. The optical rotation may depend on the frequency (RP dispersion) and undergo reversion (anomalous RP dispersion) [87–89]. It also finds interesting applications in chiral metamaterials [90–92], chiral semimetals [93,94], in the determination of the rotation direction of pulsars [95], and in rotating plasmas, which constitutes a scenario where RP sign reversal also takes place [96]. Recently, RP reversal was also reported in a bi-isotropic dielectric in the presence of chiral magnetic current [97]. Furthermore, in the presence of absorption, dichroism is another useful tool for the optical characterization of matter. It occurs when LCP and RCP light waves are absorbed by the medium at different degrees. It has been used to distinguish between Dirac and Weyl semimetals [98], perform enantiomeric discrimination [99,100], and for developing graphene-based devices at terahertz frequencies [101].

Another feature of chiral systems is the possible occurrence of negative refraction and negative refractive index, which was first proposed by Veselago in 1968 [102] and experimentally observed in 2000 [103,104]. Later, other experiments confirmed the negative refraction by using Snell's law [105,106]. This unusual property was achieved in constructed metamaterials with both negative-electric permittivity and magnetic permeability [107,108]. The negative refractive index also appears in quark-gluon plasmas [109,110], magnetoelectric materials [111], metasurfaces [112], chiral bi-anisotropic

metamaterials [113,114], and new materials, such as Dirac semimetals [115,116]. In chiral plasmas described by generalized bi-isotropic constitutive relations [117,118], the negative refractive index can occur within some frequency band and is not necessarily associated with simultaneously negative electric permittivity and negative magnetic permeability, being attributed to the chirality parameter introduced in the constitutive relations,

$$D^i = \varepsilon_{ij}E^j + i\xi_c B^i, \qquad H^i = \mu^{-1}B^i + i\xi_c E^i, \quad (9)$$

where ε_{ij}, μ, and ξ_c are the plasma electric permittivity tensor, the magnetic permeability, and the constant chirality parameter. Plasmas metamaterials have been investigated as new media endowed with interesting properties, such as negative refraction and nonlinearities [119,120]. Rotating plasmas constitute a scenario in which the birefringence is enhanced, with special properties on the RP and attenuation [121]. Therefore, plasmas provide a rich framework for theoretical and experimental investigation on the optical behavior of chiral systems, as the one developed in this work.

In this work, we are interested in examining the wave propagation in a magnetized cold plasma ruled by the MCFJ model, a chiral route distinct from the bi-isotropic/anisotropic electrodynamics of the relations (9). We carry out our analysis considering the timelike Lorentz-violating background component, which plays the role of the chiral magnetic conductivity. Such a choice is analog to the coupling with a cold axion field, for which $\nabla\theta = \mathbf{0}$, as stated in Eq. (4). The refractive indices and dispersion relations are evaluated, representing altered collective electromagnetic modes. For the propagation along the magnetic field axis, in the low-frequency limit, there appear RCP and LCP helicons, due to the presence of the chiral factor V_0. Optical effects, such as birefringence and dichroism, are examined, which could be useful to trace analogies with other material properties. We also find that the chiral conductivity yields negative refraction in specific frequency bands, amplifying the rotatory power and dichroism signals.

This paper is outlined as follows. In Sec. II, we briefly review some aspects of the MCFJ model. In Sec. III, the main properties of propagation in usual cold magnetized plasmas are presented. The dispersion relations, refractive indices, and helicons for cold plasma in chiral electrodynamics are adressed in Sec. IV. In Sec. V, we discuss the case of propagation orthogonal to the magnetic field. The optical effects are examined in Sec. VI. Finally, we summarize our results in Sec. VII.

II. BASICS ON MCFJ ELECTRODYNAMICS

The Carroll-Field-Jackiw model was proposed as a gauge invariant CPT-odd electrodynamics constrained by birefringence data of distant galaxies [42]. It was later incorporated as the CPT-odd sector of the SME [43], and it has been investigated in several respects [44,45]. In matter, it is described by the following Lagrangian density [57][1]:

$$\mathcal{L} = -\frac{1}{4}G^{\mu\nu}F_{\mu\nu} - \frac{1}{4}\epsilon^{\mu\nu\alpha\beta}(k_{AF})_\mu A_\nu F_{\alpha\beta} - A_\mu J^\mu, \quad (10)$$

yielding the MCFJ equation of motion,

$$\partial_\rho G^{\rho\kappa} + \epsilon^{\beta\kappa\mu\nu}(k_{AF})_\beta F_{\mu\nu} = J^\kappa. \quad (11)$$

Here, $(k_{AF})^\mu = (k^0_{AF}, \mathbf{k}_{AF})$ is a constant 4-vector background responsible for the Lorentz violation, and

$$F_{\mu\nu} = \partial_\mu A_\nu - \partial_\nu A_\mu, \qquad G^{\mu\nu} = \frac{1}{2}\chi^{\mu\nu\alpha\beta}F_{\alpha\beta}, \quad (12)$$

are the usual $U(1)$ vacuum and continuous matter field strength, respectively. The 4-rank tensor, $\chi^{\mu\nu\alpha\beta}$, describes the medium constitutive tensor [122], whose components provide the electric and magnetic responses of the medium. Indeed, the electric permittivity and magnetic permeability tensor components are written as $\epsilon_{ij} \equiv \chi^{0ij0}$ and $\mu^{-1}_{lk} \equiv \frac{1}{4}\epsilon_{ijl}\chi^{ijmn}\epsilon_{mnk}$, respectively. For isotropic polarization and magnetization, it holds $\epsilon_{ij} = \epsilon\delta_{ij}$ and $\mu^{-1}_{ij} = \mu^{-1}\delta_{ij}$, providing the usual isotropic constitutive relations,

$$\mathbf{D} = \epsilon\mathbf{E}, \qquad \mathbf{H} = \mu^{-1}\mathbf{B}. \quad (13)$$

A straightforward calculation from Eq. (11) yields

$$\nabla\cdot\mathbf{D} = J^0 - \mathbf{k}_{AF}\cdot\mathbf{B}, \quad (14)$$

$$\nabla\times\mathbf{H} - \frac{\partial\mathbf{D}}{\partial t} = \mathbf{J} + k^0_{AF}\mathbf{B} + \mathbf{k}_{AF}\times\mathbf{E}, \quad (15)$$

where $G^{i0} = D^i$ and $G^{ij} = -\epsilon_{ijk}H^k$. The homogeneous Maxwell equations are given by

$$\nabla\cdot\mathbf{B} = 0, \qquad \nabla\times\mathbf{E} + \frac{\partial\mathbf{B}}{\partial t} = \mathbf{0}. \quad (16)$$

By using a plane-wave ansatz for the electromagnetic fields, the MCFJ equations (14)–(16) read,

$$i\mathbf{k}\cdot\mathbf{D} + \mathbf{k}_{AF}\cdot\mathbf{B} = J^0, \quad (17a)$$

$$i\mathbf{k}\times\mathbf{H} + i\omega\mathbf{D} - k^0_{AF}\mathbf{B} - \mathbf{k}_{AF}\times\mathbf{E} = \mathbf{J}, \quad (17b)$$

$$\mathbf{k}\cdot\mathbf{B} = 0, \qquad \mathbf{k}\times\mathbf{E} - \omega\mathbf{B} = \mathbf{0}, \quad (17c)$$

where $\mathbf{k}$ is the wave vector and ω is the (angular) wave frequency.

[1]We use natural units $h = c = 1$ and the Minkowski metric signature $g_{\mu\nu} = \mathrm{diag}(1,-1,-1,-1)$.

In the presence of anisotropy, the permittivity and permeability are represented by rank 2 tensors, ε_{ij} and μ_{ij}, which may also depend on the frequency (for a dispersive medium). For an anisotropic medium, the constitutive relations (13) are replaced by [1,2],

$$D^i = \varepsilon_{ij}(\omega)E^j, \qquad B^i = \mu_{ij}(\omega)H^j. \tag{18}$$

For nonmagnetic media with isotropic magnetic permeability, it holds $\mu_{ij}(\omega) = \mu_0$, where μ_0 is the vacuum permeability. Considering the constitutive relations (18), the modified Ampère-Maxwell's law, Eq. (17b), and Faraday's law, Eq. (17c), in the absence of sources, we obtain a modified wave equation for the electric field,

$$k^i(k^jE^j) - k^2E^i = -\omega^2\mu_0\bar{\varepsilon}_{ij}(\omega)E^j, \tag{19}$$

where we define the extended permittivity tensor,

$$\bar{\varepsilon}_{ij}(\omega) = \varepsilon_{ij}(\omega) + i\frac{k^0_{AF}}{\omega^2}\epsilon_{ikj}k^k + i\epsilon_{ikj}\frac{k^k_{AF}}{\omega}. \tag{20}$$

Using the definition to the refractive index, $\mathbf{n} = \mathbf{k}/\omega$, the modified wave equation becomes

$$M_{ij}E^j = 0, \tag{21}$$

with M_{ij} given by

$$M_{ij} = n^2\delta_{ij} - n_in_j - \frac{\varepsilon_{ij}}{\varepsilon_0} - \frac{i}{\omega}(V_0\epsilon_{ikj}n^k + \epsilon_{ikj}V^k), \tag{22}$$

in which ε_0 is the vacuum electric permittivity, and

$$V_0 = k^0_{AF}/\varepsilon_0, \qquad V^k = k^k_{AF}/\varepsilon_0, \tag{23}$$

appear as the components of a redefined background, $V^\mu = (V_0, V^i)$. The nontrivial solutions for the electric field require a vanishing determinant of the matrix M_{ij}, $\det M_{ij} = 0$, which provides the dispersion relations that describe the wave propagation in the medium.

In this work, we will study plasma waves propagation for a chiral (parity-odd) medium, which means restraining our investigation to the case of a purely timelike Lorentz-violating background vector, $(k_{AF})^\mu = (k^0_{AF}, \mathbf{0})$, which also plays the role of chiral magnetic conductivity. This choice is physically meaningful since it represents cold dark matter, for which the space variation of the axion field can be neglected, $\nabla\theta = \mathbf{k}_{AF} = 0$. In this scenario, the wave equation (21) becomes

$$\left[n^2\delta_{ij} - n^in^j - \frac{\varepsilon_{ij}}{\varepsilon_0} - i\frac{V_0}{\omega}\epsilon_{ikj}n^k\right]E^j = 0. \tag{24}$$

III. THE USUAL MAGNETIZED COLD PLASMA

In this work we will adopt the fluid theory approach in the cold plasma limit [3–5,7,8]:

$$\frac{\partial n}{\partial t} + \nabla\cdot(n\mathbf{u}) = 0, \tag{25}$$

$$\frac{\partial \mathbf{u}}{\partial t} + \mathbf{u}\cdot\nabla\mathbf{u} = \frac{q}{m}(\mathbf{E} + \mathbf{u}\times\mathbf{B}_0), \tag{26}$$

where n is the electron number density, $\mathbf{u}$ is the electron fluid velocity field, q and m are the electron charge and mass, respectively, and $\mathbf{B}_0$ is the equilibrium magnetic field. For simplicity, the ions are supposed to be infinitely massive, which is appropriate for high-frequency waves. Furthermore, thermal and collisional effects are also disregarded. The linearized version of the magnetized cold plasmas [8] consider fluctuations around average quantities, n_0 and $\mathbf{B}_0$, which are constant in time and space. Thus, the plasma quantities read

$$n = n_0 + \delta n, \tag{27a}$$

$$\mathbf{u} = \delta\mathbf{u}, \tag{27b}$$

$$\mathbf{E} = \delta\mathbf{E} \tag{27c}$$

$$\mathbf{B} = \mathbf{B}_0 + \delta\mathbf{B}, \tag{27d}$$

with δn, $\delta\mathbf{u}$, $\delta\mathbf{E}$ and $\delta\mathbf{B}$ being first-order plane wave magnitude perturbations. Following the usual procedure [3–5,7], assuming $\mathbf{B}_0 = B_0\hat{z}$, we write the corresponding dielectric tensor,

$$\varepsilon_{ij}(\omega) = \varepsilon_0\begin{bmatrix} S & -iD & 0 \\ iD & S & 0 \\ 0 & 0 & P \end{bmatrix}, \tag{28}$$

where

$$S = 1 - \frac{\omega_p^2}{(\omega^2 - \omega_c^2)}, \qquad D = \frac{\omega_c\omega_p^2}{\omega(\omega^2 - \omega_c^2)}, \qquad P = 1 - \frac{\omega_p^2}{\omega^2}, \tag{29}$$

and

$$\omega_p = \frac{n_0q^2}{m\epsilon_0}, \qquad \omega_c = \frac{|q|B_0}{m}, \tag{30}$$

are the plasma and cyclotron frequencies, respectively.

In cold magnetized plasmas, it is usual to investigate modes that propagate parallel and perpendicular to the magnetic field. For longitudinal propagation to the

magnetic field, $\mathbf{k}\|\mathbf{B}_0$, two distinct refractive indices are obtained,

$$n_\pm = \sqrt{1 - \frac{\omega_p^2}{\omega(\omega \pm \omega_c)}}, \tag{31}$$

which provide left-circularly polarized and right-circularly polarized modes, respectively,

$$\mathbf{E}_{\mathrm{LCP}} = \frac{i}{\sqrt{2}}\begin{bmatrix}1\\ i\end{bmatrix}, \qquad \mathbf{E}_{\mathrm{RCP}} = \frac{i}{\sqrt{2}}\begin{bmatrix}1\\ -i\end{bmatrix}, \tag{32}$$

for the propagating modes associated to $n_\pm$, respectively. This is the standard result of wave propagation in the usual magnetized cold plasma. We recall that a cutoff happens whenever the refractive index, n, goes to zero. On the other hand, a resonance occurs if n tends to infinity. From the indices (31), we obtain the following cutoff frequencies:

$$\omega_\pm = \frac{1}{2}\left(\sqrt{\omega_c^2 + 4\omega_p^2} \mp \omega_c\right), \tag{33}$$

where $\omega_\pm$ is related to $n_\pm$, respectively.

As for perpendicular propagation to the magnetic field, $\mathbf{k}\perp\mathbf{B}_0$, $\mathbf{k} = (k_x, k_y, 0)$, two refractive indices are obtained. The one corresponding to the transversal mode, with $\delta\mathbf{E} = (0, 0, \delta E_z)\perp\mathbf{k}$, is

$$n_T^2 = P, \tag{34}$$

while the *extraordinary* mode [8],

$$n_O^2 = \frac{(S+D)(S-D)}{S}, \tag{35}$$

is longitudinal, that is, $\delta\mathbf{E} = (\delta E_x, \delta E_y, 0)$. The parameters P, S and D are given in Eq. (29). The refractive index n_T provides a linearly polarized mode, whereas n_O, in general, is related to an elliptically polarized mode.

A very usual effect in magnetized plasmas is the circular birefringence,[2] which causes the rotation of the plane of polarization of a linearly polarized wave that propagates within the medium. Thus the linearly polarized wave emerges from the medium with an electric field whose polarization is rotated relative to its initial linear configuration. Such a phenomenon can be properly explained by decomposing the initial wave into two circularly polarized waves (RCP and LCP) that travel with different phase velocities. In this case, the rotation angle of the electric field can be expressed as the difference between the refractive indices associated with the RCP and LCP waves [69,73],

$$\theta = \frac{\pi L}{\lambda_0}(\mathrm{Re}[n_{\mathrm{RCP}}] - \mathrm{Re}[n_{\mathrm{LCP}}]), \tag{36}$$

where λ_0 is the vacuum wavelength of the incident wave. The rotation power $\delta = \theta/L$ (phase difference per unit length), is given as

$$\delta = -\frac{\omega}{2}(\mathrm{Re}[n_{\mathrm{LCP}}] - \mathrm{Re}[n_{\mathrm{RCP}}]). \tag{37}$$

For parallel propagation in a cold magnetized plasma, $\mathbf{k}\|\mathbf{B}_0$, the refractive indices (31) provide the following rotatory power:

$$\delta = -\frac{\omega}{2}\mathrm{Re}\left(\sqrt{1 - \frac{\omega_p^2}{\omega(\omega+\omega_c)}} - \sqrt{1 - \frac{\omega_p^2}{\omega(\omega-\omega_c)}}\right). \tag{38}$$

The behavior of the RP (38) in terms of the frequency ω is depicted in Fig. 1. One notices that there is a divergence at ω_c, being positive for $\omega < \omega_c$ and negative for $\omega > \omega_c$. It tends to zero at the high-frequency limit $\omega \gg (\omega_p, \omega_c)$, where it decays as

$$\delta \approx -\frac{\omega_p^2 \omega_c}{2\omega^2}. \tag{39}$$

Associated with the imaginary part of the refractive index, one can also examine dichroism, an optical effect that occurs when circularly polarized waves are absorbed by the medium at different degrees [57,59,60]. Thus dichroism coefficient refers to the difference in absorption of LCP and RCP waves, being given by

$$\delta_d = -\frac{\omega}{2}(\mathrm{Im}[n_{\mathrm{LCP}}] - \mathrm{Im}[n_{\mathrm{RCP}}]), \tag{40}$$

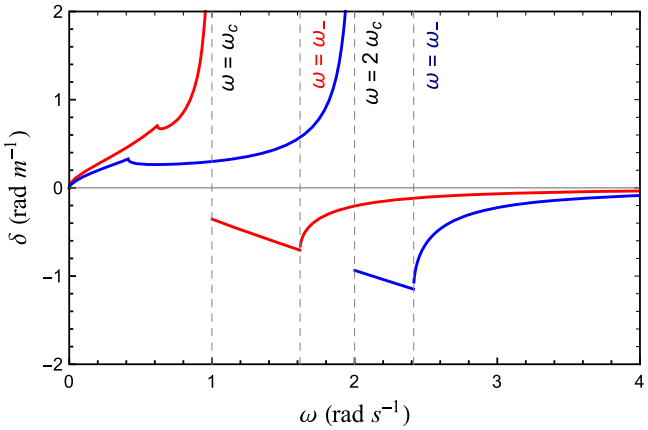

FIG. 1. Rotatory power (38) in terms of ω. Here, $\omega_c = \omega_p$ (red line) and $\omega_c = 2\omega_p$ (blue line), with the choice $\omega_c = 1$ rad s^{-1}.

[2]In plasmas, the birefringence is usually a consequence of the Faraday effect, occurring due to the presence of the external field $\mathbf{B}_0$, which generates distinct phase velocities for the propagating modes [71].

which, for the refractive indices (31), implies

$$\delta_d = -\frac{\omega}{2}\mathrm{Im}\left(\sqrt{1-\frac{\omega_p^2}{\omega(\omega+\omega_c)}}-\sqrt{1-\frac{\omega_p^2}{\omega(\omega-\omega_c)}}\right). \quad (41)$$

Such a quantity is plotted in Fig. 2, which shows singularity at the cyclotron frequency ω_c. For $\omega_c = \omega_p$ (red curve), the dichroism coefficient (41) is negative for $\omega < \omega_+^{\mathrm{red}}$, positive for $2\omega_c < \omega < \omega_-^{\mathrm{red}}$ and null for other frequencies. The case for $\omega_c = \omega_p/2$ (blue curve) differs in the fact that ω_+^{blue} is greater than ω_c, showing that (41) is now negative for $\omega < \omega_c$.

IV. WAVE PROPAGATION IN CHIRAL PLASMA ALONG THE MAGNETIC FIELD

Collective modes of chiral systems were examined in the context of the Weyl materials by means of the chiral kinetic theory [123]. Using a similar formalism, low-energy collective modes (pseudomagnetic helicons) were predicted for Dirac and Weyl matter [124]. In this section, we derive the collective electromagnetic modes of the cold chiral plasma ruled by the permittivity (20). In this sense, we start from the wave equation (24) and use the expression of the magnetized plasma dielectric permittivity, given in Eq. (28), obtaining a linear homogeneous system,

$$\begin{bmatrix} n^2-n_x^2-S & iD-n_xn_y+i(V_0/\omega)n_z & -n_xn_z-i(V_0/\omega)n_y \\ -iD-n_xn_y-i(V_0/\omega)n_z & n^2-n_y^2-S & -n_yn_z+i(V_0/\omega)n_x \\ -n_xn_z+i(V_0/\omega)n_y & -n_yn_z-i(V_0/\omega)n_x & n^2-n_z^2-P \end{bmatrix}\begin{bmatrix}\delta E_x\\ \delta E_y\\ \delta E_z\end{bmatrix} = 0. \quad (42)$$

Let us consider, for simplicity, the case the refractive index is parallel to the magnetic field, $\mathbf{n} = n\hat{z}$, such that one obtains

$$\begin{bmatrix} n^2-S & iD+i(V_0/\omega)n & 0 \\ -iD-i(V_0/\omega)n & n^2-S & 0 \\ 0 & 0 & -P \end{bmatrix}\begin{bmatrix}\delta E_x\\ \delta E_y\\ \delta E_z\end{bmatrix} = 0, \quad (43)$$

for which $\det[M_{ij}] = 0$ provides the dispersion relations

$$P(\omega^2(n^2-S)^2-(\omega D+nV_0)^2) = 0. \quad (44)$$

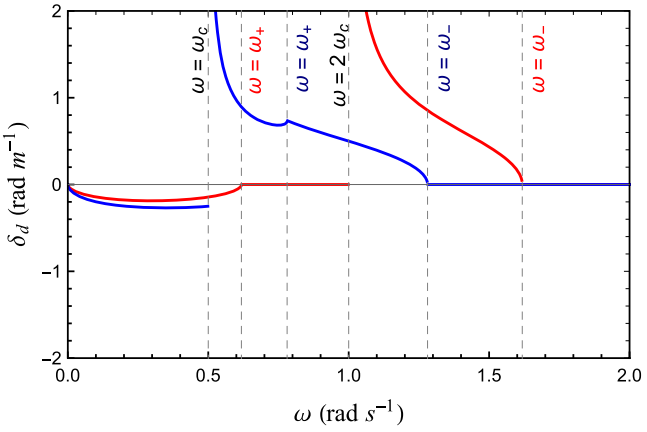

FIG. 2. Dichroism coefficient (41) in terms of ω. Here, $\omega_c = \omega_p$ (red line) and $\omega_c = \omega_p/2$ (blue line), with $\omega_c = 1$ rad s^{-1}.

Longitudinal waves, $\mathbf{n}\|\delta\mathbf{E}$ or $\delta\mathbf{E} = (0,0,\delta E_z)$, may emerge, when $P = 0$, with nonpropagating vibration at the plasma frequency, $\omega = \omega_p$. Under an electromagnetic perspective, this longitudinal oscillation is a plasmon. In a solid-state context, the collective mode of electrons vibrating (longitudinally) under the action of the electromagnetic field is also called plasmons.

For transverse waves, $\mathbf{n}\perp\delta\mathbf{E}$ or $\delta\mathbf{E} = (\delta E_x, \delta E_y, 0)$, the dispersion relation (44) simplifies as

$$(n^2-S)^2-(D+n(V_0/\omega))^2 = 0, \quad (45)$$

also written as a fourth-order equation in n,

$$n^4-(2S+(V_0/\omega)^2)n^2-2D(V_0/\omega)n+(S^2-D^2) = 0. \quad (46)$$

Taking into account the relations (29), the dispersion relation (46) provides the following refractive indices for electromagnetic modes of the model:

$$n_{R,M} = -\frac{V_0}{2\omega}\pm\sqrt{1+\left(\frac{V_0}{2\omega}\right)^2-\frac{\omega_p^2}{\omega(\omega-\omega_c)}}, \quad (47)$$

$$n_{L,E} = \frac{V_0}{2\omega}\pm\sqrt{1+\left(\frac{V_0}{2\omega}\right)^2-\frac{\omega_p^2}{\omega(\omega+\omega_c)}}. \quad (48)$$

In general, the indices n_R, n_L, n_E, n_M may be real, imaginary, or complex (presenting both pieces) at some frequency ranges. As well-known, the real part is associated with propagation, while the complex piece is

concerned with absorption. Furthermore, these indices may have positive or negative real pieces. The indices n_L and n_M are always positive and negative, respectively, the latter one being a negative refractive index. On the other hand, the indices n_R and n_E can be positive or negative, depending on the frequency zone examined, in such a way the associated modes can manifest negative refraction behavior (in a suitable frequency band).

The propagating modes associated with the refractive indices in Eq. (47) and Eq. (48) are obtained by inserting each one in Eq. (43) and carrying out the corresponding eigenvector (with a null eigenvalue). The emerging electric field are the $\mathbf{E}_{\mathrm{LCP}}$ and $\mathbf{E}_{\mathrm{RCP}}$, given in Eq. (32), where n_R, n_M are associated with the RCP mode, and n_L, n_E are related to the LCP mode,

$$n_L, n_E \mapsto \mathbf{E}_{\mathrm{LCP}} = \frac{i}{\sqrt{2}}\begin{bmatrix}1\\ i\end{bmatrix}, \tag{49}$$

$$n_R, n_M \mapsto \mathbf{E}_{\mathrm{RCP}} = \frac{i}{\sqrt{2}}\begin{bmatrix}1\\ -i\end{bmatrix}. \tag{50}$$

From the indices n_R, n_E, given by Eqs. (47) and (48), we obtain the same cutoff frequencies (33) of the standard case: in fact, ω_- is related to the refractive index n_R, and ω_+ is associated with the refractive index n_E. In contrast, the refractive indices n_L and n_M have no real root. The behavior of the refractive indices in Eqs. (47) and (48) will be examined in the following.

A. About the index n_R

We initiate discussing some properties of the index n_R. The behavior of n_R in terms of the dimensionless parameter ω/ω_c is illustrated in Fig. 3, which displays the real imaginary pieces of the refractive index n_R. We point out:

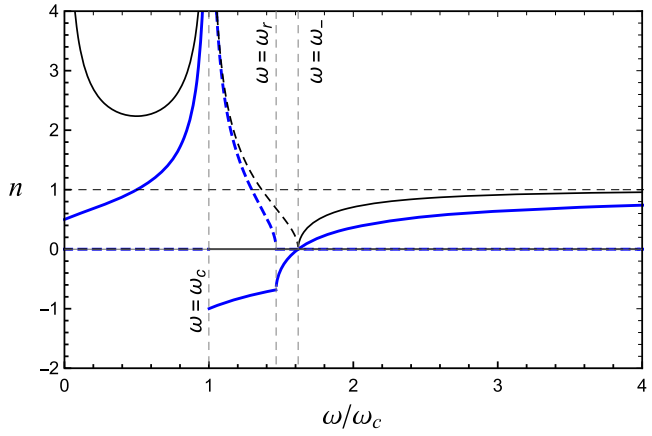

FIG. 3. Index of refraction n_R in terms of the frequency ω. The dashed blue (black) line corresponds to the imaginary piece of n_R (n_-), while the solid blue (black) line represents the real piece of n_R (n_-). Here $\omega_c = \omega_p$, $V_0 = 2\omega_p$, and $\omega_c = 1$ rad s^{-1}.

(i) It takes on a finite value when $\omega \to 0$, given by

$$n_R(0) = \frac{1}{V_0}\left(\frac{\omega_p^2}{\omega_c}\right), \tag{51}$$

describing a modified helicon in relation to the standard scenario, where the usual magnetized index n_- goes to infinity near the origin.

(ii) For $0 < \omega < \omega_c$, n_R is positive since the square root in (47) is real, positive, and larger than the negative piece before it. Such a positivity also holds for the usual index n_-. See the black line in this frequency zone in Fig. 3.

(iii) For $\omega \to \omega_c$, $n_R \to \infty$, and there occurs a resonance at the cyclotron frequency.

(iv) For $\omega_c < \omega < \omega_r$, there appears a negative refractive index zone with absorption, where $\mathrm{Re}[n_R] < 0$ and $\mathrm{Im}[n_R] \neq 0$, as shown in Fig. 3. The frequency ω_r is the root of the radicand in Eq. (47),

$$R_-(\omega) = 1 + \frac{V_0^2}{4\omega^2} - \frac{\omega_p^2}{\omega(\omega-\omega_c)}, \tag{52}$$

which yields a cubic equation in ω.

(v) For $\omega_r < \omega < \omega_-$, one finds a negative refractive index zone without absorption, that is, $\mathrm{Re}[n_R] < 0$ and $\mathrm{Im}[n_R] = 0$.

(vi) For $\omega > \omega_-$, the quantity n_R is always positive, corresponding to a propagating zone, with $n_R \to 1$ in the high-frequency limit.

The frequency zone in which $\mathrm{Im}[n_R] \neq 0$, that is, $\omega_c < \omega < \omega_r$, corresponds to the absorption zone for the metamaterial (negative refractive index) RCP wave, as already mentioned before. The frequency ranges in which $\mathrm{Im}[n_R] = 0$ define the propagation zone for the RCP wave.

B. About the index n_L

The index n_L, given in Eq. (48), has no real root, presenting the following features:

(i) For $\omega \to 0$, $n_L \to +\infty$. Then, the presence of the term V_0 turns the refractive index real and positively divergent at the origin, differing from the usual index n_+ behavior, see Eq. (31), which is complex and divergent, $\mathrm{Im}[n_+] \to \infty$, at the origin. As it will be clear in Eq. (60) of Sec. E, this index also supports helicons, or more specifically, LCP helicons.

(ii) For $\omega > 0$, it is necessary to analyze the radicand in Eq. (48),

$$R_+(\omega) = 1 + \frac{V_0^2}{4\omega^2} - \frac{\omega_p^2}{\omega(\omega+\omega_c)}, \tag{53}$$

since it can be positive or negative, which determines the absence or presence of an absorption zone, respectively. Note that for $\omega > \omega_+$ the term

$1-\omega_p^2/\omega(\omega+\omega_c)$ is greater than zero (ω_+ is the root of such a term), such that R_+ is positive. Therefore, the possibility of R_+ being negative occurs only in the range $0<\omega<\omega_+$, for which the term $1-\omega_p^2/\omega(\omega+\omega_c)$ is less than zero. Hence, this positivity for R_+ is stated by the condition,

$$\frac{V_0^2}{4\omega^2} > \left|1-\frac{4\omega_p^2}{\omega(\omega+\omega_c)}\right|_{\omega<\omega_+}, \tag{54}$$

for which R_+ is always positive and the refractive index n_L is real for any $\omega>0$. This corresponds to a propagating mode for the entire frequency domain. The behavior of n_L in terms of the dimensionless parameter ω/ω_c, considering the condition (54), that is, $R_+>0$, is shown in Fig. 4.

(iii) On the other hand, for

$$\frac{V_0^2}{4\omega^2} < \left|1-\frac{4\omega_p^2}{\omega(\omega+\omega_c)}\right|_{\omega<\omega_+}, \tag{55}$$

one has $R_+<0$ and n_L becomes complex, $\mathrm{Im}[n_L]\neq 0$, determining the opening of an absorption zone located within the interval $\omega_i<\omega<\omega_f$, as shown in Fig. 5. The frequencies ω_i and ω_f are positive and real roots of R_+, a cubic equation in the frequency.

C. About the index n_E

The quantity n_E is a refractive index that only exists as a positive quantity due to the presence of the chiral Lorentz-violating term. In the case we set $V_0=0$, the second relation in Eq. (48) yields $\mathrm{Re}[n_E]<0$ (negative index of refraction). For $V_0\neq 0$, the index n_E presents a small positivity range, $\mathrm{Re}[n_E]>0$, which provides propagation

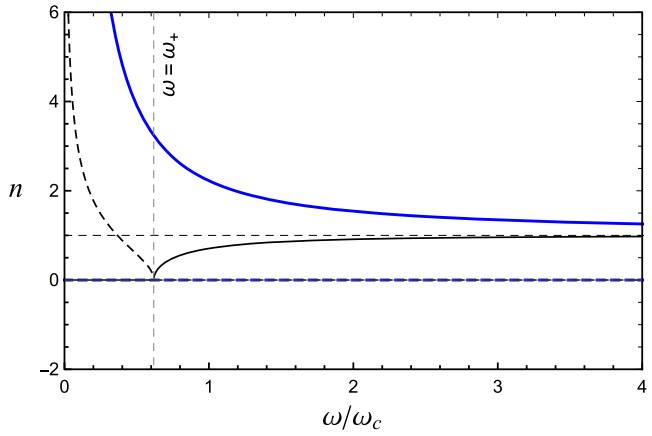

FIG. 4. Refractive index n_L (blue lines) for the condition (54), $R_+>0$. Refractive index n_+ (black lines) of Eq. (31). The dashed (solid) lines correspond to the imaginary (real) pieces of n_L and n_+. Here $\omega_c=\omega_p$, $V_0=2\omega_p$, and $\omega_c=1\ \mathrm{rad\,s^{-1}}$.

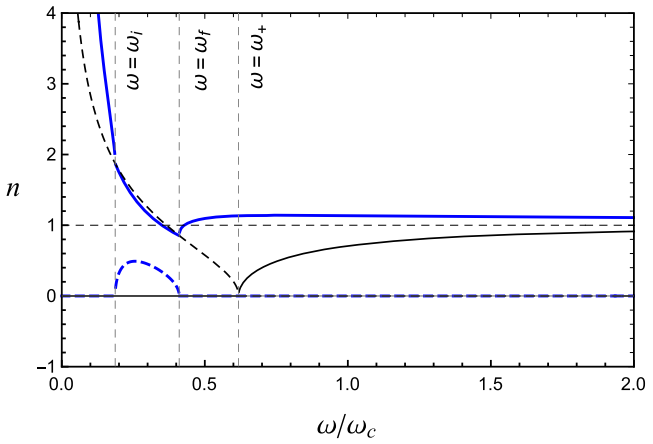

FIG. 5. Refractive index n_L (blue lines) for the condition (55), $R_+<0$. Refractive index n_+ (black lines) of Eq. (31). The dashed (solid) lines correspond to the imaginary (real) pieces of n_L and n_+. Here $\omega_c=\omega_p$, $V_0=0.7\omega_p$, and $\omega_c=1\ \mathrm{rad\,s^{-1}}$.

for the associated LCP wave. We present below some aspects of n_E:

(i) For $\omega\to 0$, the index n_E tends to a finite value at origin,

$$n_E(0)=\frac{1}{V_0}\left[\frac{\omega_p^2}{\omega_c}\right], \tag{56}$$

which is inversely proportional to the magnitude of the chiral factor, V_0. Such a distinct low-frequency behavior also implies a LCP helicon, inexistent in the usual case.

(ii) Since the radicand of n_E is the same one of n_L, see Eq. (48), it holds here the same procedure applied for n_L. For values of V_0 that satisfy the condition

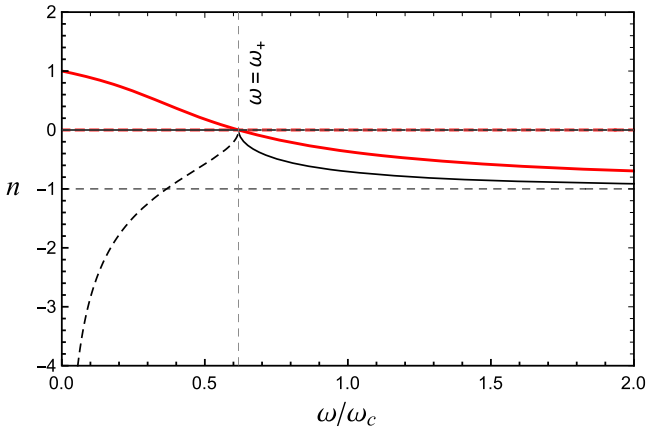

FIG. 6. Red line: plot of the index n_E for the condition (54), $R_+>0$. Black line: plot of the index $-n_+$ of Eq. (31). Dashed (solid) lines represent the imaginary (real) pieces of n_E and $-n_+$. Here, we have used $\omega_c=\omega_p$ and $V_0=2\omega_p$, with the choice $\omega_c=1\ \mathrm{rad\,s^{-1}}$.

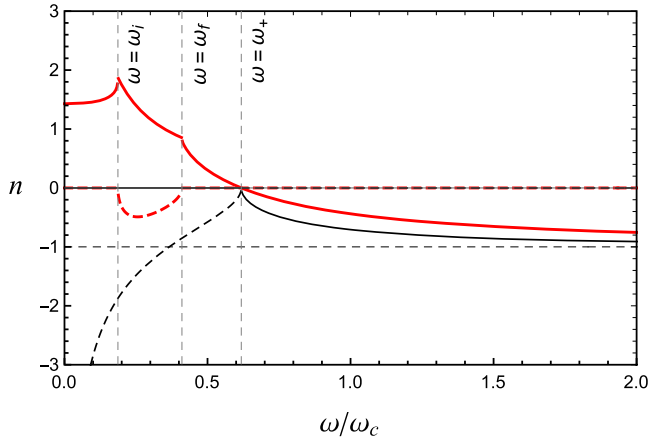

FIG. 7. Red line: plot of the index n_E for the condition (55), $R_+ < 0$. Black line: plot of the index $-n_+$ of Eq. (31). Dashed (solid) lines represent the imaginary (real) pieces of n_E and $-n_+$. Here, we have set $\omega_c = \omega_p$, $V_0 = 0.7\omega_p$, and $\omega_c = 1$ rad s^{-1}.

(54), $R_+ > 0$, n_E is always real, $\mathrm{Im}[n_E] = 0$, being positive within the interval $0 < \omega < \omega_+$, and negative for $\omega > \omega_+$, since $\sqrt{R_+} > V_0/2\omega$ at this range. The real and imaginary parts of n_E are represented in Fig. 6.

(iii) Considering the condition (55), n_E becomes complex and exhibits an absorption zone, $\mathrm{Im}[n_E] \neq 0$, in the interval $\omega_i < \omega < \omega_f$, with $\omega_i, \omega_f < \omega_+$, as shown in Fig. 7. Such a figure depicts the real and imaginary pieces of n_E [under the condition (55)].

D. About the index n_M

The additional index n_M, given in Eq. (47), is always negative (negative refraction) and has no real root. The behavior of n_M in terms of the dimensionless parameter ω/ω_c is shown in Fig. 8. We notice the following features:

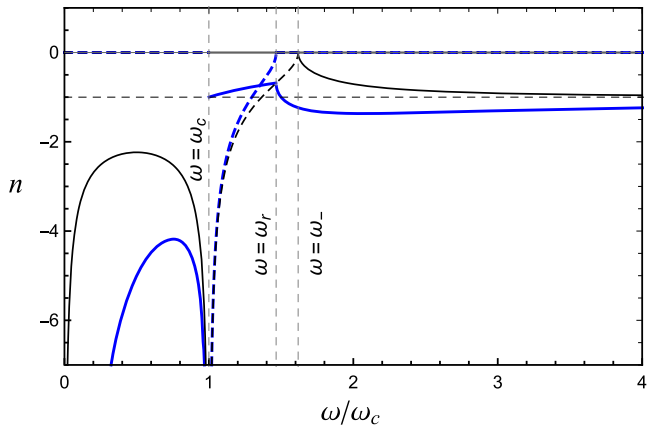

FIG. 8. Blue line: plot of the index n_M. Black line: plot of the real piece of $-n_-$ of Eq. (31). Dashed (solid) lines represent the imaginary (real) pieces of n_M and $-n_-$. Here, we have used: $\omega_c = \omega_p$, $V_0 = 2\omega_p$, and $\omega_c = 1$ rad s^{-1}.

(i) For $0 < \omega < \omega_c$, n_M is real and negative since the square root in (47) is real. This is the same behavior of the index $-n_-$. See the black line in Fig. (8).

(ii) For $\omega \to \omega_c$, $n_M \to -\infty$, and there occurs a resonance at the cyclotron frequency.

(iii) For $\omega_c < \omega < \omega_r$, there appears an absorption zone for metamaterial, $\mathrm{Re}[n_M] < 0$ and $\mathrm{Im}[n_M] \neq 0$, while the index $-n_-$ is purely imaginary, $\mathrm{Re}[n_M] = 0$ and $\mathrm{Im}[n_M] \neq 0$, as shown in Fig. 8. The frequency ω_r is the root of R_-.

(iv) For $\omega > \omega_r$, the quantity n_M is always negative, corresponding to a negative propagation zone, with $n_M \to -1$ in the high-frequency limit.

E. Low-frequency modes

Considering the low-frequency regime,

$$\omega \ll \omega_p, \qquad \omega_c \ll \omega_p, \qquad \omega \ll \omega_c, \tag{57}$$

the magnetized plasma RCP refractive index (31) provides a helicon mode, described by

$$n_- = \omega_p \sqrt{\frac{1}{\omega\omega_c}}. \tag{58}$$

Helicons are RCP modes that propagate at very low frequencies and along the magnetic field axis. See Ref. [5] (Chapter 9), and Ref. [6] (Chapter 8) for basic details.

For the electromagnetic modes obtained in Eq. (47) and Eq. (48), the corresponding helicons indices are

$$\bar{n}_{R,E} = \frac{\omega_p^2}{\omega_c V_0}, \tag{59}$$

$$\bar{n}_{L,M} = -\frac{\omega_p^2}{\omega_c V_0} \pm \frac{V_0}{\omega}, \tag{60}$$

where we have used the "bar" notation to indicate the helicons quantities. In this chiral context, we observe the existence of both RCP and LCP helicons, that both propagate in the low-energy regime, due to the presence of the timelike component, V_0. The helicon modes given by $\bar{n}_{R,E}$ have constant and nondispersive indices, which depend on the inverse of V_0. On the other hand, negative-refraction dispersive helicons are associated with $\bar{n}_M$, and also with $\bar{n}_L$ for $\omega < \omega_c V_0^2/\omega_p^2$. Note that the term V_0/ω appears as a channel of distinction between the helicons associated with $\bar{n}_{R,E}$ and $\bar{n}_{L,M}$, as expected.

The cold plasma usual helicon mode is recovered if one also considers, besides the relations (57), the condition $V_0 \ll \omega$. In this case, the expansion of $n_{R,E}$ of Eq. (47) and $n_{L,M}$ of Eq. (48) yields

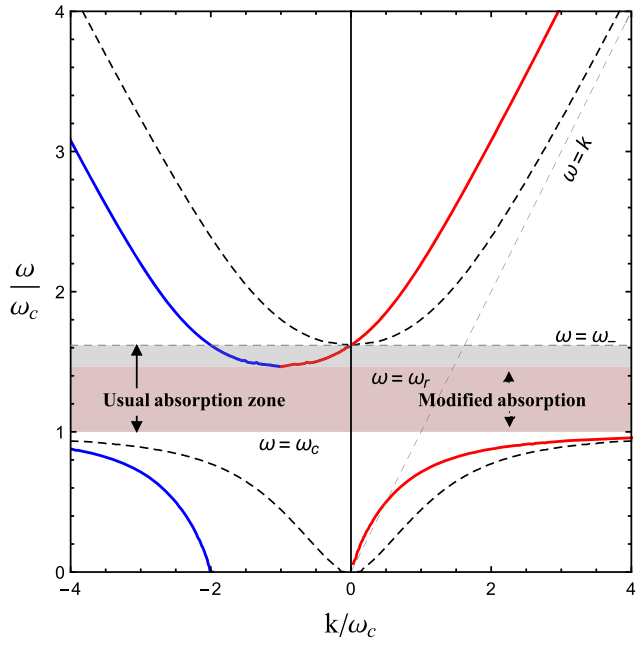

FIG. 9. Plot of the dispersion relations related to refractive indices n_R (solid red line) and n_M (solid blue line). The dashed black line corresponds to the indices of the usual case ($\pm n_-$). The highlighted area in red (gray) indicates the absorption zone for $n_{R,M}$ ($\pm n_-$). Here, we have used $\omega_c = \omega_p$ and $V_0 = 2\omega_p$, with $\omega_c = 1$ rad s^{-1}.

$$\tilde{n}_{R,M} = \pm\omega_p\sqrt{\frac{1}{\omega\omega_c}}, \tag{61}$$

which is the same result as the usual case [see Eq. (58)], and $\tilde{n}_{L,E}$ being purely imaginary. Here, the "tilde" notation indicates helicons in the specific case where $\omega_c \ll \omega_p$, $\omega \ll \omega_c$, and $V_0 \ll \omega$.

F. Dispersion relations behavior

The wave dispersion associated with each refractive index is usually visualized in plots $\omega \times k$. In the following, we work with dimensionless plots, $(\omega/\omega_c) \times (k/\omega_c)$.

The dispersion relations associated with n_R and n_M are depicted in Fig. 9 for $\omega_c = \omega_p$. The propagation occurs for $0 < \omega < \omega_c$ and $\omega > \omega_-$, while absorption takes place in $\omega_c < \omega < \omega_r$. The range $\omega_r < \omega < \omega_-$ corresponds to negative refraction propagation zone ($k < 0$) for n_R. The refractive index n_M is negative for $k < 0$ and $\omega > 0$.

Figure 10 depicts the dispersion relations related to n_L and n_E. The wave associated with n_L propagates for all frequencies. For n_E, the conventional propagation zone occurs in $0 < \omega < \omega_+$. For $\omega > \omega_+$, there occurs a propagation zone with negative refraction. For the standard indices, $\pm n_+$, the absorption zone is $0 < \omega < \omega_+$.

Furthermore, Fig. 11 shows the dispersion relations for n_L and n_E in the case there is a modified absorption zone for $\omega_i < \omega < \omega_f$, while the free propagation occurs for

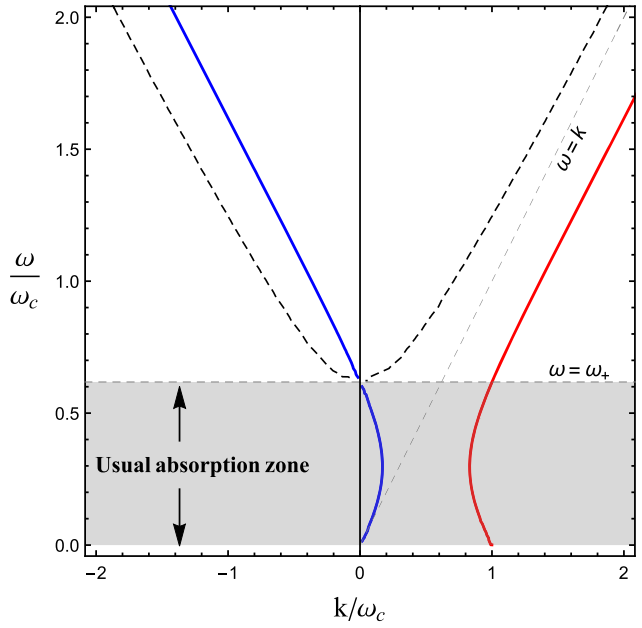

FIG. 10. Plot of the dispersion relations related to refractive indices n_L (solid red line) and n_E (solid blue line). The dashed line corresponds to the indices $\pm n_+$ of the usual case. The highlighted gray area indicates the absorption zone for $\pm n_+$, where now also occurs propagation. Here, we have used $\omega_c = \omega_p$ and $V_0 = \omega_p$, with $\omega_c = 1$ rad s^{-1}.

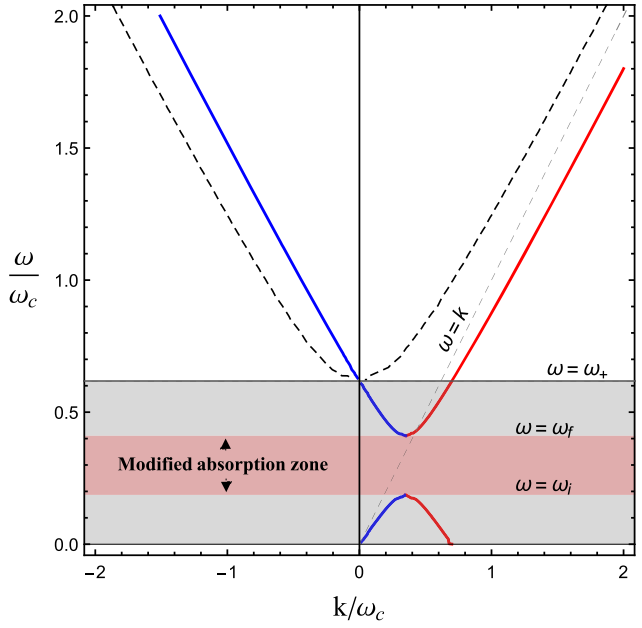

FIG. 11. Plot of the dispersion relations related to refractive indices n_L (solid red line) and n_E (solid blue line). The dashed line corresponds to the usual case with indices $\pm n_+$. The highlighted areas in red (gray) indicate the absorption zone for $n_{L,E}$ ($\pm n_+$). Here, we have used $\omega_c = \omega_p$ and $V_0 = 0.7\omega_c$, with $\omega_c = 1$ rad s^{-1}.

$0 < \omega < \omega_i$ and $\omega > \omega_f$. The frequencies ω_i, ω_f, and ω_r define the limits for unusual propagation zones. As already discussed, these frequencies are obtained from the radicands (52) and (53).

V. WAVE PROPAGATION ORTHOGONAL TO THE MAGNETIC FIELD

For investigating wave propagation orthogonally to the magnetic field direction, we rewrite Eq. (42) for $\mathbf{n} = (n_x, n_y, 0)$, that is,

$$\begin{bmatrix} n^2 - n_x^2 - S & iD - n_x n_y & -i(V_0/\omega)n_y \\ -iD - n_x n_y & n^2 - n_y^2 - S & +i(V_0/\omega)n_x \\ +i(V_0/\omega)n_y & -i(V_0/\omega)n_x & n^2 - P \end{bmatrix} \begin{bmatrix} \delta E_x \\ \delta E_y \\ \delta E_z \end{bmatrix} = 0. \tag{62}$$

Using the parametrization $\mathbf{n} = n(\cos\phi, \sin\phi, 0)$, it becomes

$$\begin{bmatrix} n^2 - n^2\cos^2\phi - S & iD - n^2\sin\phi\cos\phi & -i(V_0/\omega)n\sin\phi \\ -iD - n^2\sin\phi\cos\phi & n^2 - n^2\sin^2\phi - S & +i(V_0/\omega)n\cos\phi \\ +i(V_0/\omega)n\sin\phi & -i(V_0/\omega)n\cos\phi & n^2 - P \end{bmatrix} \begin{bmatrix} \delta E_x \\ \delta E_y \\ \delta E_z \end{bmatrix} = 0, \tag{63}$$

whose null determinant yields the angle-independent dispersion relation,

$$\frac{n^2 S V_0^2}{\omega^2} - (n^2 - P)(D^2 + S(n^2 - S)) = 0, \tag{64}$$

providing two refractive indices given by

$$n_{O\pm}^2 = \frac{P+S}{2} - \frac{D^2}{2S} + \frac{V_0^2}{2\omega^2} \pm \frac{\Gamma}{2S}, \tag{65}$$

where

$$\Gamma = \sqrt{\left(D^2 - PS - S^2 - \frac{SV_0^2}{\omega^2}\right)^2 - 4SP(S^2 - D^2)}. \tag{66}$$

From Eq. (63), the indices in Eq. (65) are related to the following propagating modes:

$$\mathbf{E} = C \begin{bmatrix} \zeta \\ 1 \\ i\frac{SV_0 n_{O\pm}}{\gamma\omega(n_{O\pm}^2 - P)} \end{bmatrix}, \tag{67}$$

with

$$C = \frac{\omega(n_{O\pm}^2 - P)|\gamma|}{\sqrt{2\omega^2(n_{O\pm}^2 - P)^2|\gamma|^2 + (SV_0 n_{O\pm})^2}}, \tag{68}$$

$$\zeta = -\frac{S\sin\phi - iD\cos\phi}{\gamma}, \tag{69}$$

$$\gamma = S\cos\phi + iD\sin\phi. \tag{70}$$

The refractive index n_{O+} has a cutoff at the plasma frequency ω_p, while n_{O-} has two cutoff frequencies, $\omega_\pm$, given in Eq. (33).

A. About the index n_{O+}

The refractive index n_{O+} has to be compared to the index n_T, given in Eq. (34), associated with the usual transversal mode, since in the limit $V_0 \to 0$ it recovers the refractive index n_T. We present below some aspects of n_{O+}:

(i) For $0 < \omega < \omega_p$, there is a propagation zone in which n_{O+} is real. This behavior is markedly different from the usual case, for which there corresponds to an absorption zone (in this range). See the dashed black line in Fig. 12.

(ii) For $\omega \to \omega_p$, n_{O+} has an unusual discontinuity, as shown in Fig. 12 (see the red curve).

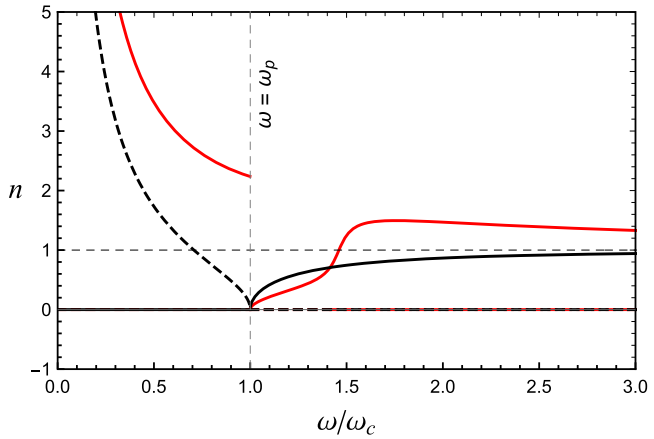

FIG. 12. Red line: plot of the index n_{O+}. Black line: plot of the index n_T. Dashed (solid) lines represent the imaginary (real) pieces of n_{O+} and n_T. Here, we have used: $\omega_c = \omega_p$, $V_0 = 2\omega_p$, and $\omega_c = 1$ rad s^{-1}.

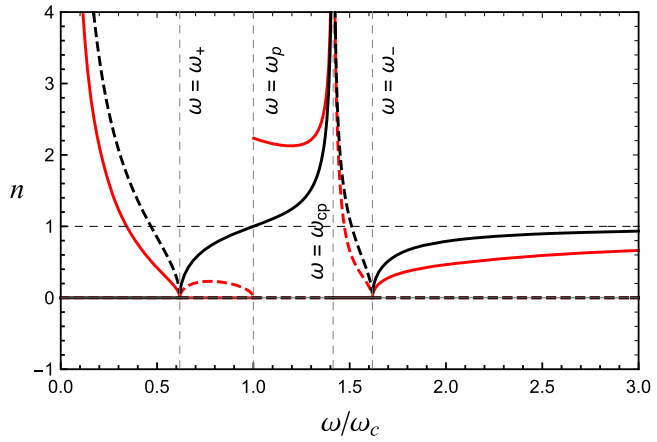

FIG. 13. Red line: plot of the index n_{O-}. Black line: plot of the index n_O. Dashed (solid) lines represent the imaginary (real) pieces of n_{O-} and n_{O-}. Here, we have used $\omega_c = \omega_p$, $V_0 = 2\omega_p$, and $\omega_c = 1$ rad s^{-1}.

(iii) For $\omega > \omega_p$, the index n_{O+} is always real, corresponding to a propagation zone.

B. About the index n_{O-}

The refractive index n_{O-}, given in Eq. (65), is a modification of the index (35), associated with the usual extraordinary mode. The index n_{O-} shares the same usual resonance frequency,

$$\omega_{cp} = \sqrt{\omega_c^2 + \omega_p^2}. \tag{71}$$

We point out:

(i) For $0 < \omega < \omega_+$, n_{O-} is real and positive, corresponding to a propagation zone. It contrasts with the usual case, where n_O is imaginary in this range (absorption zone). See the black line in Fig. 13.

(ii) For $\omega_+ < \omega < \omega_p$, there occurs an absorption zone, where $\mathrm{Re}[n_{O-}] = 0$ and $\mathrm{Im}[n_{O-}] \neq 0$. In the standard case, there is a propagation zone in this range.

(iii) For $\omega \to \omega_p$, n_{O-} has a discontinuity, as shown in Fig. 13. For $\omega_p < \omega < \omega_{cp}$, the index n_{O-} is real and there appears a propagation zone. The same positivity occurs in the usual case.

(iv) For $\omega \to \omega_{cp}$, the index $n_{O-} \to +\infty$ and there occurs a resonance. For $\omega_{cp} < \omega < \omega_-$, $\mathrm{Re}[n_{O-}] = 0$ and $\mathrm{Im}[n_{O-}] \neq 0$, and one has an absorption zone, the same behavior of the usual case in this range.

(v) For $\omega > \omega_-$, the quantity n_{O-} is always positive, corresponding to a propagation zone.

VI. BIREFRINGENCE, ROTATORY POWER AND DICHROISM

The phase velocity in terms of the refractive index n is defined (in natural units) as $v_{\mathrm{phase}} = 1/n$. Hence, the corresponding phase velocities, $v_R = 1/(n_R)$, $v_L = 1/(n_L)$, $v_E = 1/(n_E)$, $v_M = 1/(n_M)$, can be defined with the indices n_R, n_L, n_E, n_M of Eqs. (47) and (48). Accordingly with the previous analysis of the refractive indices, in general, the RCP and LCP modes propagate at different phase velocities for each frequency value, generating circular birefringence in the propagation band, expressed in terms of the rotatory power (37). On the other hand, in the absorption zones, there occurs dichroism, measured in terms of the coefficient of Eq. (40).

A. Rotatory power

In order to write the rotatory power, we need to consider the refractive indices n_L, n_E, associated with the LCP wave, and the indices n_R, n_M, associated to the RCP wave. It allows, in principle, to determine four distinct RPs at the propagation zones, some of which we examine in this section.

We start by writing the rotation power defined in terms of real pieces of the refractive indices n_L and n_R,

$$\delta_{LR} = -\frac{\omega}{2}(\mathrm{Re}[n_L] - \mathrm{Re}[n_R]), \tag{72}$$

or explicitly,

$$\delta_{LR} = -\frac{\omega}{2}\mathrm{Re}\left[V_0/\omega + \sqrt{R_+} - \sqrt{R_-}\right], \tag{73}$$

where R_+ and R_- are given in Eqs. (52) and (53). We find a positive frequency,

$$\hat{\omega} = \sqrt{\omega_c^2 + \omega_p^2/2 - \frac{\omega_p^2\sqrt{4\omega_c^2 + V_0^2}}{2V_0}}, \tag{74}$$

where the RP (73) undergoes a sign reversal. In Fig. 14, we illustrate the behavior of RP for the condition (54). For the interval $0 < \omega < \hat{\omega}$, the RP is negative, and for $\hat{\omega} < \omega < \omega_c$, it is positive. The RP reversion that occurs at $\omega = \hat{\omega}$ is not usual in cold plasmas theory. However, it is reported in graphene systems [85], rotating plasmas [96], and bi-isotropic dielectrics supporting chiral magnetic current [97]. For $\omega > \omega_c$, the RP is always negative. Nevertheless, it is necessary to pay attention to the interval $\omega_c < \omega < \omega_r$, where the refractive index n_R has an imaginary piece and the RCP wave is absorbed. At $\omega = \omega_r$, the real piece of n_R undergoes a sharp change (see Fig. 3), which also appears in the RP profile of Fig. 14.

We can safely claim that both modes associated with the n_L and n_R propagate for $\omega > \omega_-$, range in which the RP magnitude decreases monotonically with ω, approaching to its asymptotic value, $-V_0/2$ (see Fig. 14). Assuming the limit where $\omega \gg (\omega_p, \omega_c)$, we can write

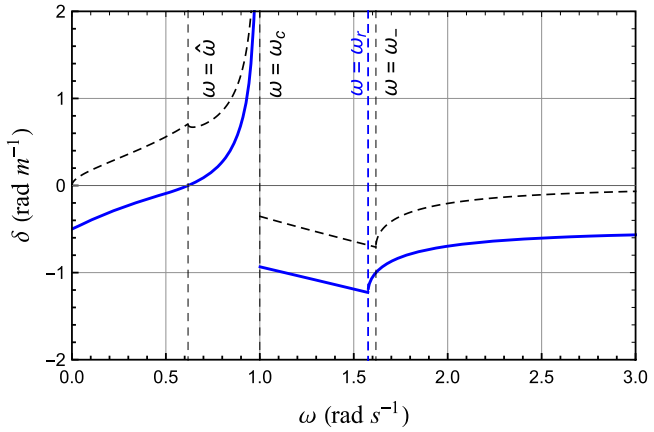

FIG. 14. The solid blue line represents the rotatory power (73) defined by the refractive index n_L and n_R, for the condition (54). The dashed black line corresponds to the usual rotatory power (38). Here, we have used $\omega_c = \omega_p$, $V_0 = \omega_p$, and $\omega_c = 1$ rad s^{-1}.

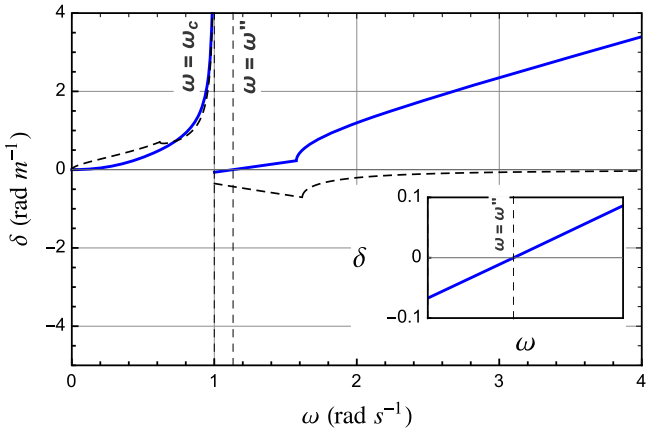

FIG. 15. Solid blue lines: plot of the rotatory power (79) associated to the refractive indices n_E and n_R for the condition (54). The dashed line represents the usual rotatory power (38). Here, we have used $\omega_c = \omega_p$, $V_0 = \omega_p$, and $\omega_c = 1$ rad s^{-1}. The inset plot highlights the behavior of δ around $\omega = \omega''$.

$$n_{L,R} \approx 1 \pm \frac{V_0}{2\omega} + \frac{V_0^2}{8\omega^2} - \frac{\omega_p^2}{2\omega(\omega \pm \omega_c)}, \tag{75}$$

so that the rotatory power is

$$\delta_{LR} \approx -\frac{V_0}{2} - \frac{\omega_p^2 \omega_c}{2\omega^2}. \tag{76}$$

Note that taking the limit $V_0 \to 0$, the usual Faraday effect RP (39) is recovered for the high-frequency regime. It is also interesting to point out that the Faraday effect disappears for a null magnetic field, $\omega_c = 0$. However, the birefringence still remains, due to the presence of the chiral term, which yields the following RP:

$$\delta \approx -V_0/2. \tag{77}$$

For the condition (55), the RP (73) also exhibits a sign reversal and a very similar profile to the one of Fig. 14, in such a way that it will not be depicted here.

Considering now the refractive indices n_E and n_R, the rotatory power is

$$\delta_{\mathrm{ER}} = -\frac{\omega}{2}(\mathrm{Re}[n_E] - \mathrm{Re}[n_R]), \tag{78}$$

or,

$$\delta_{\mathrm{ER}} = -\frac{\omega}{2}\mathrm{Re}\left[V_0/\omega - \sqrt{R_+} - \sqrt{R_-}\right]. \tag{79}$$

Recalling that the LCP wave associated with n_E has a conventional free propagation for $\omega < \omega_+$ and propagation with negative refractive index ($n_E < 0$) for $\omega > \omega_+$ (with $\omega_+ < \omega_c$), the RP magnitude is enhanced in the latter zone. This behavior is depicted in Fig. 15, which shows the RP (79) for n_E given by the condition (54), $R_+ > 0$. The RP is positive for $\omega < \omega_c$ and negative for $\omega_c < \omega < \omega''$, becoming positive again for $\omega > \omega''$, where ω'' is the reversal frequency. For n_E given by the condition condition (55), the RP is depicted in Fig. 16, revealing a small reversion at $\omega'' < \omega_c$. Note that the increasing RP with ω, depicted in Figs. 15 and 16, is due to the negative behavior of the index n_E for $\omega > \omega_+$, that is, enhancement associated with the negative refraction.

In the asymptotic limit, where $\omega \gg (\omega_p, \omega_c)$, the RP (79) goes as

$$\delta_{\mathrm{ER}} \approx \omega - \frac{V_0}{2}, \tag{80}$$

presentig a predominant linear behavior in ω, as it appears in Figs. 15 and 16. It is also worth mentioning that the limit

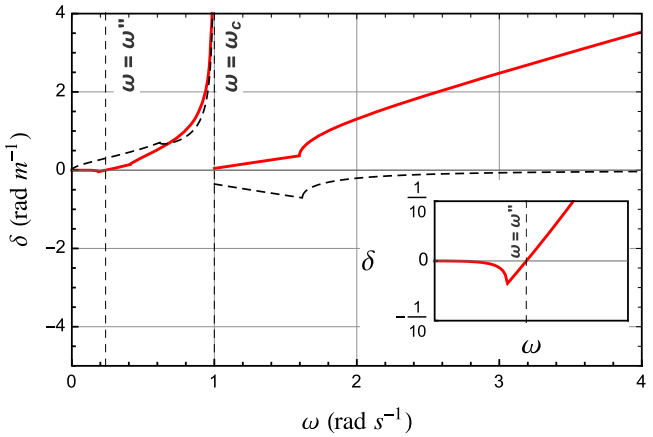

FIG. 16. Solid red lines: rotatory power (79) associated to the refractive indices n_E and n_R for the condition (55). The dashed line represents the usual rotatory power (38). Here, we have used $\omega_c = \omega_p$, $V_0 = 0.7\omega_p$, and $\omega_c = 1$ rad s^{-1}. The inset plot highlights the behavior of δ around $\omega = \omega''$.

$V_0 \to 0$, implying $\delta \approx \omega$, does not stand for a valid result for usual magnetized plasma, since the RP (79) is not defined for achiral cold plasmas.

B. Dichroism coefficients

As well known, absorption depends on the magnitude of the imaginary parts of the refractive indices. When one mode is more absorbed than the other, there occurs dichroism. Considering the refractive indices n_L and n_R, the circular dichroism coefficient is

$$\delta_{dLR} = -\frac{\omega}{2}(\mathrm{Im}[n_L] - \mathrm{Im}[n_R]). \tag{81}$$

Considering the condition (54), only n_R has imaginary part (localized in the interval $\omega_c < \omega < \omega_-$), while n_L is real for $\omega > 0$. In this case, the dichroism coefficient is given by

$$\delta_{dLR} = \begin{cases} 0, & \text{for } 0 < \omega < \omega_c, \\ \sqrt{R_-}, & \text{for } \omega_c < \omega < \omega_r, \\ 0, & \text{for } \omega > \omega_r, \end{cases} \tag{82}$$

being non-null only in the range $\omega_c < \omega < \omega_-$, as properly shown in Fig. 17.

Considering the condition (55), both n_R and n_L have non-null imaginary parts in the intervals $\omega_c < \omega < \omega_r$ and $\omega_i < \omega < \omega_f$, respectively. The dichroism coefficient is null for $0 < \omega < \omega_i$, $\omega_f < \omega < \omega_c$, and $\omega > \omega_r$, being non-null only for

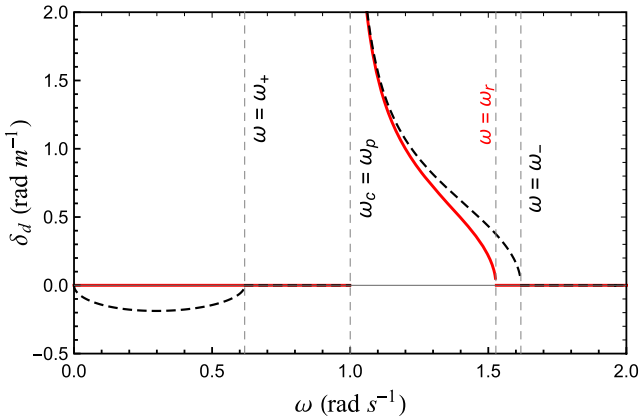

FIG. 17. Plot of the dichroism coefficient (82) (red solid lines) associated to the refractive indices n_L and n_R, under the condition (54). The black dashed line represents the usual dichroism coefficient (41). Here $\omega_c = \omega_p$, $V_0 = (3/2)\omega_c$, and $\omega_c = 1$ rad s^{-1}.

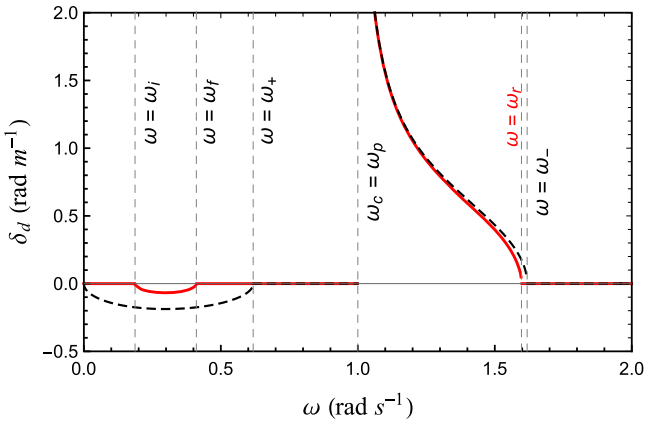

FIG. 18. Plot of the dichroism coefficient (83) (solid red lines) associated to the refractive indices n_L and n_R, under the condition (55). The dashed line represents the usual dichroism coefficient (41). Here, we have set $\omega_c = \omega_p$, $V_0 = 0.7\omega_p$, and $\omega_c = 1$ rad s^{-1}.

$$\delta_{dLR} = \begin{cases} -\frac{\omega}{2}\sqrt{R_+}, & \text{for } \omega_i < \omega < \omega_f, \\ +\frac{\omega}{2}\sqrt{R_-}, & \text{for } \omega_c < \omega < \omega_r, \end{cases} \tag{83}$$

whose general behavior is exhibited in Fig. 18.

For the refractive indices n_E and n_R, the circular dichroism coefficient is

$$\delta_{dER} = -\frac{\omega}{2}(\mathrm{Im}[n_E] - \mathrm{Im}[n_R]). \tag{84}$$

If we consider n_E under the condition (54), the same behavior of Fig. 17 is obtained, since n_E is always real, not contributing to the dichroism. On the other hand, regarding the condition (55), both n_R e n_E have nonzero imaginary parts in the intervals $\omega_c < \omega < \omega_r$ and $\omega_i < \omega < \omega_f$, respectively. In this case, we have

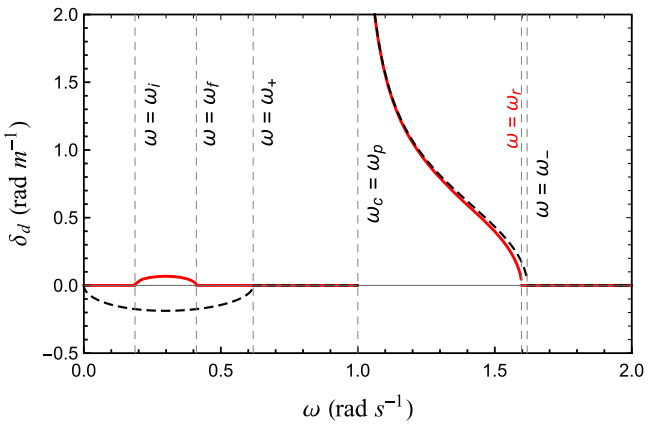

FIG. 19. Plot of the dichroism coefficients (85) associated to the refractive indices n_E and n_R [for the condition (55)]. The dashed line represents the usual dichroism coefficient (41). Here, we have used $\omega_c = \omega_p$, $V_0 = 0.7\omega_p$, and $\omega_c = 1$ rad s^{-1}.

$$\delta_{dER}=\begin{cases}0, & \text{for } 0<\omega<\omega_i,\\ +\frac{\omega}{2}\sqrt{R_+}, & \text{for } \omega_i<\omega<\omega_f,\\ 0, & \text{for } \omega_f<\omega<\omega_c,\\ +\frac{\omega}{2}\sqrt{R_-}, & \text{for } \omega_c<\omega<\omega_r,\\ 0, & \text{for } \omega>\omega_r.\end{cases} \tag{85}$$

The general behavior of the dichroism coefficient (85) is illustrated in Fig. 19.

VII. FINAL REMARKS

In this work, we have examined the propagation of electromagnetic waves in a cold magnetized plasma in the context of the chiral MCFJ electrodynamics, describing the implied optical effects as well. We have adopted a MCFJ timelike background vector in order to represent the chirality factor that breaks the parity. Starting from the modified Maxwell equations and employing the usual methods, the wave propagation along the magnetic field axis was firstly examined, yieldind the four modified refractive indices given by Eqs. (47) and (48), associated with circularly polarized propagating modes. Such indices were analyzed in detail in the Secs. IV A–IV D, where some of them exhibited significant modifications, as the index n_R, see Fig. 3. It presents a negative refraction behavior in the range $\omega_c<\omega<\omega_-$, in which it occurs propagation with absorption for $\omega_c<\omega<\omega_r$ and free (metamaterial) propagation for $\omega_r<\omega<\omega_-$. The usual counterpart index presents only pure absorption in this range. The low-frequency limit was investigated, there appearing propagating RCP and LCP helicons due to the presence of the chiral factor, V_0. Wave propagation orthogonally to the magnetic field was also investigated in Sec. V, providing refractive indices and propagating modes modified by V_0.

Optical effects for the propagating modes along the magnetic field, involving birefringence and dichroism, were discussed in Sec. VI, considering the refractive index n_L and n_R and n_E. In Sec. VI A, the RP δ_{LR} was introduced, see Eq. (73), exhibiting sign reversion at $\omega=\hat{\omega}$, for the conditions (54) and (55). The RP δ_{ER} also exhibits sign change at $\omega=\omega''>\omega_c$ for the condition (54), and $\omega=\omega''<\omega_c$ under the condition (55), as shown in Figs. 15 and 16, respectively. The RP also increases with the frequency for $\omega>\omega_c$. The reported RP reversal is not usual in cold plasmas, being reported in graphene systems [85], rotating plasmas [96], Weyl metals and semimetals with low electron density with chiral conductivity [93,94], and bi-isotropic dielectrics with magnetic chiral conductivity [97]. Comparing our results with the rotating plasma scenario of Ref. [96], there appear differences. In the rotating plasma, the RP undergoes reversal and decays as $1/\omega^2$ for high frequencies. In the present case, the rotatory power tends to the asymptotical value $-V_0$, see Eq. (77), or increases with ω when it involves the negative refraction index, see Eq. (80). These distinct RP properties may provide a channel to optically characterize chiral cold plasmas, being of experimental interest.

Besides the nonconventional effect of reversion, the RP can also be enhanced when it is defined in the negative refraction zone. Such an enhancement occurs for δ_{ER}, given in Eq. (79), for $\omega>\omega_+$ (zone in which n_E is negative), being a topic of interest in metamaterial plasmas [117–120]. Dichroism was examined in Sec. VI B, where the coefficients δ_{dLR} and δ_{dER} have been shown to be non-null only in the range $\omega_c<\omega<\omega_r$, for the condition (54)—see Figs. 17, and in the intervals $\omega_c<\omega<\omega_r$, $\omega_i<\omega<\omega_f$, for the condition (55), in accordance with Figs. 18 and 19.

For a cold-axion dark matter, $\nabla\theta=\mathbf{0}$, it holds $\nabla\times\mathbf{B}-\partial_t\mathbf{E}=\mathbf{j}+V_0\mathbf{B}$, with $V_0=\partial_t\theta$, related to time dependence of the axion field. If one considers V_0 constant, one has an effective chiral electrodynamics in the background of an axion field, as discussed in Sec. XI of Ref. [125]. This is the scenario addressed in the present manuscript. On the other hand, a plasma interacting with a vibrating cold axion dark matter with frequency ω_a is an interesting problem that may open nice connections between cold plasmas and axion/dark matter systems, including the possibility of experiments involving dielectric haloscopes [126] and tunable plasmas haloscopes [127,128].

ACKNOWLEDGMENTS

The authors express their gratitude to FAPEMA, CNPq, and CAPES (Brazilian research agencies) for their invaluable financial support. M. M. F. is supported by FAPEMA Universal/01187/18, CNPq/Produtividade 311220/2019-3 and CNPq/Universal/422527/2021-1. P. D. S. S is supported by FAPEMA BPD-12562/22. Furthermore, we are indebted to CAPES/Finance Code 001 and FAPEMA/POS- GRAD-02575/21.

[1] A. Zangwill, *Modern Electrodynamics* (Cambridge University Press, New York, 2012).
[2] J. D. Jackson, *Classical Electrodynamics*, 3rd ed. (John Wiley & Sons, New York, 1999).
[3] D. A. Gurnett and A. Bhattacharjee, *Introduction to Plasma Physics* (Cambridge University Press, Cambridge, 2005).
[4] P. A. Sturrock, *Plasma Physics: An Introduction to the Theory of Astrophysical, Geophysical and Laboratory*

Plasmas (Cambridge University Press, Cambridge, England, 1994).
[5] J. A. Bittencourt, *Fundamentals of Plasma Physics*, 3rd ed. (Springer, New York, 2004).
[6] P. Chabert and N. Braithwaite, *Physics of Radio-Frequency Plasmas* (Cambridge University Press, Cambridge, 2011).
[7] T. H. Stix, *Waves in Plasmas* (Springer, New York, 1992).
[8] T. J. M. Boyd and J. J. Sanderson, *The Physics of plasmas* (Cambridge University Press, New York, 2003).
[9] A. Piel, *Plasmas Physics—An Introduction to Laboratory, Space, and Fusion Plasmas* (Springer, Heidelberg, 2010).
[10] E. V. Appleton and G. Builder, The ionosphere as a doubly refracting medium., Proc. Phys. Soc. **45**, 208 (1932); E. V. Appleton, Wireless studies of the ionosphere, J. Inst. Electr. Eng. **7**, 257 (1932).
[11] D. R. Hartree, The propagation of electromagnetic waves in a stratified medium, Math. Proc. Cambridge Philos. Soc. **25**, 97 (1929).
[12] J. A. Ratcliff, The formation of the ionosphere. Ideas of the early years (1925-1955)., J. Atmos. Terr. Phys. **36**, 2167 (1974).
[13] F. Haas, P. Gaete, L. P. R. Ospedal, and José Abdalla Helayël-Neto, Modified plasma waves described by a logarithmic electrodynamics, Phys. Plasmas **26**, 042108 (2019).
[14] D. E. Kharzeev, The chiral magnetic effect and anomaly-induced transport, Prog. Part. Nucl. Phys. **75**, 133 (2014); D. E. Kharzeev, J. Liao, S. A. Voloshin, and G. Wang, Chiral magnetic and vortical effects in high-energy nuclear collisions—A status report, Prog. Part. Nucl. Phys. **88**, 1 (2016).
[15] D. Kharzeev, K. Landsteiner, A. Schmitt, and H. U. Yee, *Strongly Interacting Matter in Magnetic Fields*, Lecture Notes in Physics Vol. 871 (Springer-Verlag, Berlin·Heidelberg, 2013).
[16] K. Fukushima, D. E. Kharzeev, and H. J. Warringa, Chiral magnetic effect, Phys. Rev. D **78**, 074033 (2008); D. E. Kharzeev and H. J. Warringa, Chiral magnetic conductivity, Phys. Rev. D **80**, 034028 (2009).
[17] Q. Li, D. E. Kharzeev, C. Zhang, Y. Huang, I. Pletikosić, A. V. Fedorov, R. D. Zhong, J. A. Schneeloch, G. D. Gu, and T. Valla, Chiral magnetic effect in $ZrTe_5$, Nat. Phys. **12**, 550 (2016).
[18] A. Vilenkin, Equilibrium parity-violating current in a magnetic field, Phys. Rev. D **22**, 3080 (1980); A. Vilenkin and D. A. Leahy, Parity nonconservation and the origin of cosmic magnetic fields, Astrophys. J. **254**, 77 (1982).
[19] G. Inghirami, M. Mace, Y. Hirono, L. Del Zanna, D. E. Kharzeev, and M. Bleicher, Magnetic fields in heavy ion collisions: Flow and charge transport, Eur. Phys. J. C **80**, 293 (2020).
[20] J. Schober, A. Brandenburg, and I. Rogachevskii, Chiral fermion asymmetry in high-energy plasma simulations, Geophys. Astrophys. Fluid Dyn. **114**, 106 (2020).
[21] Y. Akamatsu and N. Yamamoto, Chiral Plasma Instabilities, Phys. Rev. Lett. **111**, 052002 (2013); A. Boyarsky, O. Ruchayskiy, and M. Shaposhnikov, Long-Range Magnetic Fields in the Ground State of the Standard Model Plasma, Phys. Rev. Lett. **109**, 111602 (2012).
[22] M. Dvornikov and V. B. Semikoz, Influence of the turbulent motion on the chiral magnetic effect in the early universe, Phys. Rev. D **95**, 043538 (2017).
[23] G. Sigl and N. Leite, Chiral magnetic effect in protoneutron stars and magnetic field spectral evolution, J. Cosmol. Astropart. Phys. 01 (2016) 025.
[24] M. Dvornikov and V. B. Semikoz, Magnetic field instability in a neutron star driven by the electroweak electron-nucleon interaction versus the chiral magnetic effect, Phys. Rev. D **91**, 061301(R) (2015).
[25] M. Dvornikov and V. B. Semikoz, Instability of magnetic fields in electroweak plasma driven by neutrino asymmetries, J. Cosmol. Astropart. Phys. 05 (2014) 002; M. Dvornikov, Electric current induced by an external magnetic field in the presence of electroweak matter, EPJ Web Conf. **191**, 05008 (2018).
[26] A. A. Burkov, Chiral anomaly and transport in Weyl metals, J. Phys. Condens. Matter **27**, 113201 (2015).
[27] M.-C. Chang and M.-F. Yang, Chiral magnetic effect in a two-band lattice model of Weyl semimetal, Phys. Rev. B **91**, 115203 (2015).
[28] E. C. I van der Wurff and H. T. C. Stoof, Anisotropic chiral magnetic effect from tilted Weyl cones, Phys. Rev. B **96**, 121116(R) (2017).
[29] K. Landsteiner, Anomalous transport of Weyl fermions in Weyl semimetals, Phys. Rev. B **89**, 075124 (2014).
[30] S. Kaushik and D. E. Kharzeev, Quantum oscillations in the chiral magnetic conductivity, Phys. Rev. B **95**, 235136 (2017).
[31] A. Martín-Ruiz, M. Cambiaso, and L. F. Urrutia, Electromagnetic fields induced by an electric charge near a Weyl semimetal, Phys. Rev. B **99**, 155142 (2019).
[32] R. E. Throckmorton, J. Hofmann, E. Barnes, and S. D. Sarma, Many-body effects and ultraviolet renormalization in three-dimensional Dirac materials, Phys. Rev. B **92**, 115101 (2015).
[33] K. Deng, J. S. Van Dyke, D. Minic, J. J. Heremans, and E. Barnes, Exploring self-consistency of the equations of axion electrodynamics in Weyl semimetals, Phys. Rev. B **104**, 075202 (2021).
[34] E. Barnes, J. J. Heremans, and Djordje Minic, Electromagnetic Signatures of the Chiral Anomaly in Weyl Semimetals, Phys. Rev. Lett. **117**, 217204 (2016).
[35] F. Wilczek, Two Applications of Axion Electrodynamics, Phys. Rev. Lett. **58**, 1799 (1987).
[36] A. Sekine and K. Nomura, Axion electrodynamics in topological materials, J. Appl. Phys. **129**, 141101 (2021).
[37] M. E. Tobar, B. T. McAllister, and M. Goryachev, Modified axion electrodynamics as impressed electromagnetic sources through oscillating background polarization and magnetization, Phys. Dark Universe **26**, 100339 (2019).
[38] J. M. A. Paixão, L. P. R. Ospedal, M. J. Neves, and J. A. Helayël-Neto, The axion-photon mixing in non-linear electrodynamic scenarios, J. High Energy Phys. 10 (2022) 160.
[39] Z. Qiu, G. Cao, and X.-G. Huang, Electrodynamics of chiral matter, Phys. Rev. D **95**, 036002 (2017).

[40] P. D. S. Silva, M. M. Ferreira Jr., M. Schreck, and L. F. Urrutia, Magnetic-conductivity effects on electromagnetic propagation in dispersive matter, Phys. Rev. D **102**, 076001 (2020).
[41] S. Kaushik, D. E. Kharzeev, and E. J. Philip, Transverse chiral magnetic photocurrent induced by linearly polarized light in symmetric Weyl semimetals, Phys. Rev. Res. **2**, 042011(R) (2020).
[42] S. M. Carroll, G. B. Field, and R. Jackiw, Limits on a Lorentz- and parity-violating modification of electrodynamics, Phys. Rev. D **41**, 1231 (1990).
[43] D. Colladay and V. A. Kostelecký, CPT violation and the standard model, Phys. Rev. D **55**, 6760 (1997); Lorentz-violating extension of the standard model, Phys. Rev. D **58**, 116002 (1998); S. R. Coleman and S. L. Glashow, High-energy tests of Lorentz invariance, Phys. Rev. D **59**, 116008 (1999).
[44] A. A. Andrianov and R. Soldati, Lorentz symmetry breaking in Abelian vector-field models with Wess-Zumino interaction, Phys. Rev. D **51**, 5961 (1995); Patterns of Lorentz symmetry breaking in QED by CPT-odd interaction, Phys. Lett. B**435**, 449 (1998); A. A. Andrianov, R. Soldati, and L. Sorbo, Dynamical Lorentz symmetry breaking from a $(3+1)$-dimensional axion-Wess-Zumino model, Phys. Rev. D **59**, 025002 (1999).
[45] J. Alfaro, A. A. Andrianov, M. Cambiaso, P. Giacconi, and R. Soldati, Bare and induced Lorentz and CPT invariance violations in QED, Int. J. Mod. Phys. A **25**, 3271 (2010); A. A. Andrianov, D. Espriu, P. Giacconi, and R. Soldati, Anomalous positron excess from Lorentz-violating QED, J. High Energy Phys. 09 (2009) 057.
[46] L. C. T. Brito, J. C. C. Felipe, A. Yu. Petrov, and A. P. Baeta Scarpelli, No radiative corrections to the Carroll-Field-Jackiw term beyond one-loop order, Int. J. Mod. Phys. A**36**, 2150033 (2021); J. F. Assunção, T. Mariz, and A. Yu. Petrov, Nonanalyticity of the induced Carroll-Field-Jackiw term at finite temperature, Europhys. Lett. **116**, 31003 (2016); J. C. C. Felipe, A. R. Vieira, A. L. Cherchiglia, A. P. Baêta Scarpelli, and M. Sampaio, Arbitrariness in the gravitational Chern-Simons-like term induced radiatively, Phys. Rev. D **89**, 105034 (2014); T. R. S. Santos and R. F. Sobreiro, Lorentz-violating Yang–Mills theory: Discussing the Chern–Simons-like term generation, Eur. Phys. J. C **77**, 903 (2017).
[47] R. Casana, M. M. Ferreira Jr., E. da Hora, and A. B. F. Neves, Maxwell-Chern-Simons vortices in a *CPT*-odd Lorentz-violating Higgs electrodynamics, Eur. Phys. J. C **74**, 3064 (2014); R. Casana and L. Sourrouille, Self-dual Maxwell-Chern-Simons solitons from a Lorentz-violating model, Phys. Lett. B **726**, 488 (2013).
[48] H. Belich, L. D. Bernald, Patricio Gaete, and J. A. Helayël-Neto, The photino sector and a confining potential in a supersymetric Lorentz-symmetry-violating model, Eur. Phys. J. C **73**, 2632 (2013); L. Bonetti, L. R. dos Santos Filho, J A. Helayël-Neto, and A. D. A. M. Spallicci, Photon sector analysis of Super and Lorentz symmetry breaking: Effective photon mass, bi-refringence and dissipation, Eur. Phys. J. C **78**, 811 (2018).
[49] L. H. C. Borges and A. F. Ferrari, External sources in a minimal and nonminimal *CPT*-odd Lorentz violating Maxwell electrodynamics, Mod. Phys. Lett. A **37**, 2250021 (2022); Y. M. P. Gomes and P. C. Malta, Lab-based limits on the Carroll-Field-Jackiw Lorentz-violating electrodynamics, Phys. Rev. D **94**, 025031 (2016); M. M. Ferreira Jr., J. A. Helayël-Neto, C. M. Reyes, M. Schreck, and P. D. S. Silva, Unitarity in Stückelberg electrodynamics modified by a Carroll-Field-Jackiw term, Phys. Lett. B **804**, 135379 (2020); A. Martín-Ruiz and C. A. Escobar, Local effects of the quantum vacuum in Lorentz-violating electrodynamics, Phys. Rev. D **95**, 036011 (2017).
[50] V. A. Kostelecký and M. Mewes, Cosmological Constraints on Lorentz Violation in Electrodynamics, Phys. Rev. Lett. **87**, 251304 (2001); Signals for Lorentz violation in electrodynamics, Phys. Rev. D **66**, 056005 (2002); Sensitive Polarimetric Search for Relativity Violations in Gamma-Ray Bursts, Phys. Rev. Lett. **97**, 140401 (2006).
[51] F. R. Klinkhamer and M. Schreck, Consistency of isotropic modified Maxwell theory: Microcausality and unitarity, Nucl. Phys. **B848**, 90 (2011); M. Schreck, Analysis of the consistency of parity-odd nonbirefringent modified Maxwell theory, Phys. Rev. D **86**, 065038 (2012).
[52] C. A. Escobar and M. A. G. Garcia, Full CPT-even photon sector of the standard model extension at finite temperature, Phys. Rev. D **92**, 025034 (2015); A. Martín-Ruiz and C. A. Escobar, Casimir effect between ponderable media as modeled by the standard model extension, Phys. Rev. D **94**, 076010 (2016); L. H. C. Borges and A. F. Ferrari, Semi-transparent boundaries in *CPT*-even Lorentz violating electrodynamics, Nucl. Phys. **B980**, 115829 (2022).
[53] Q. G. Bailey and V. A. Kostelecký, Lorentz-violating electrostatics and magnetostatics, Phys. Rev. D **70**, 076006 (2004).
[54] A. Gómez, A. Martín-Ruiz, and Luis F. Urrutia, Effective electromagnetic actions for Lorentz violating theories exhibiting the axial anomaly, Phys. Lett. B **829**, 137043 (2022).
[55] A. V. Kostelecký, R. Lehnert, N. McGinnis, M. Schreck, and B. Seradjeh, Lorentz violation in Dirac and Weyl semimetals, Phys. Rev. Res. **4**, 023106 (2022).
[56] M. M. Ferreira Jr., L. Lisboa-Santos, R. V. Maluf, and M. Schreck, Maxwell electrodynamics modified by a CPT-odd dimension-five higher-derivative term, Phys. Rev. D **100**, 055036 (2019).
[57] P. D. S. Silva, L. L. Santos, M. M. Ferreira Jr., and M. Schreck, Effects of *CPT*-odd terms of dimensions three and five on electromagnetic propagation in continuous matter, Phys. Rev. D **104**, 116023 (2021).
[58] L. D. Barron, *Molecular Light Scattering and Optical Activity*, 2nd ed. (Cambridge University Press, New York, 2004).
[59] E. Hecht, *Optics*, 4nd ed. (Addison Wesley, San Francisco, 2002).
[60] G. H. Wagniere, *On Chirality and the Universal Asymmetry: Reflections on Image and Mirror Image* (Wiley-VCH, Zurich, 2007).
[61] Y. Tang and A. E. Cohen, Optical Chirality and Its Interaction with Matter, Phys. Rev. Lett. **104**, 163901 (2010).
[62] A. H. Sihvola and I. V. Lindell, Bi-isotropic constitutive relations, Microwave Opt. Technol. Lett. **4**, 295 (1991);

Properties of bi-isotropic Fresnel reflection coefficients, Opt. Commun. **89**, 1 (1992); S. Ougier, I. Chenerie, A. Sihvola, and A. Priou, Propagation in bi-isotropic media: Effect of different formalisms on the propagation analysis, Prog. Electromagn. Res. **09**, 19 (1994).

[63] P. Hillion, Manifestly covariant formalism for electromagnetism in chiral media, Phys. Rev. E **47**, 1365 (1993); Y. Itin, Dispersion relation for electromagnetic waves in anisotropic media, Phys. Lett. A **374**, 1113 (2010); N. J. Damaskos, A. L. Maffett, and P. L. E. Uslenghi, Dispersion relation for general anisotropic media, IEEE Trans. Antennas Propagat. **30**, 991 (1982).

[64] J. A. Kong, *Electromagnetic Wave Theory* (Wiley, New York, 1986).

[65] Y. T. Aladadi and M. A. S. Alkanhal, Classification and characterization of electromagnetic materials, Sci. Rep. **10**, 11406 (2020).

[66] W. Mahmood and Q. Zhao, The double Jones birefringence in magneto-electric medium, Sci. Rep. **5**, 13963 (2015).

[67] V. A. De Lorenci and G. P. Goulart, Magnetoelectric birefringence revisited, Phys. Rev. D **78**, 045015 (2008).

[68] P. D. S. Silva, R. Casana, and M. M. Ferreira Jr., Symmetric and antisymmetric constitutive tensors for bi-isotropic and bi-anisotropic media, Phys. Rev. A **106**, 042205 (2022).

[69] G. R. Fowles, *Introduction to Modern Optics*, 2nd ed. (Dover Publications, INC., New York, 1975); A. K. Bain, *Crystal Optics: Properties and Applications* (Wiley-VCH Verlag GmbH & Co. KGaA, Germany, 2019).

[70] H. S. Bennett and E. A. Stern, Faraday effect in solids, Phys. Rev. **137**, A448 (1965); L. M. Roth, Theory of the Faraday effect in solids, Phys. Rev. **133**, A542 (1964).

[71] W. S. Porter and E. M. Bock Jr., Faraday effect in a plasma, Am. J. Phys. **33**, 1070 (1965).

[72] J. Shibata, A. Takeuchi, H. Kohno, and G. Tatara, Theory of electromagnetic wave propagation in ferromagnetic Rashba conductor, J. Appl. Phys. **123**, 063902 (2018).

[73] E. U. Condon, Theories of optical rotatory power, Rev. Mod. Phys. **9**, 432 (1937).

[74] Ming-Che Chang and Min-Fong Yang, Optical signature of topological insulators, Phys. Rev. B **80**, 113304 (2009); L. Ohnoutek *et al.*, Strong interband Faraday rotation in 3D topological insulator Bi_2Se_3, Sci. Rep. **6**, 19087 (2016).

[75] A. Martín-Ruiz, M. Cambiaso, and L. F. Urrutia, The magnetoelectric coupling in electrodynamics, Int. J. Mod. Phys. A **34**, 1941002 (2019); A. Martín-Ruiz, M. Cambiaso, and L. F. Urrutia, Electro- and magnetostatics of topological insulators as modeled by planar, spherical, and cylindrical θ boundaries: Green's function approach, Phys. Rev. D **93**, 045022 (2016).

[76] A. Lakhtakia and T. G. Mackay, Classical electromagnetic model of surface states in topological insulators, J. Nanophoton. **10**, 033004 (2016).

[77] T. M. Melo, D. R. Viana, W. A. Moura-Melo, J. M. Fonseca, and A. R. Pereira, Topological cutoff frequency in a slab waveguide: Penetration length in topological insulator walls, Phys. Lett. A **380**, 973 (2016).

[78] Z.-X. Li, Yunshan Cao, and Peng Yan, Topological insulators and semimetals in classical magnetic systems, Phys. Rep. **915**, 1 (2021).

[79] R. Li, J. Wang, Xiao-Liang Qi, and S.-C. Zhang, Dynamical axion field in topological magnetic insulators, Nat. Phys. **6**, 284 (2010).

[80] W.-K. Tse and A. H. MacDonald, Giant Magneto-Optical Kerr Effect and Universal Faraday Effect in Thin-Film Topological Insulators, Phys. Rev. Lett. **105**, 057401 (2010); Magneto-optical and magnetoelectric effects of topological insulators in quantizing magnetic fields, Phys. Rev. B **82**, 161104 (2010); Magneto-optical Faraday and Kerr effects in topological insulator films and in other layered quantized Hall systems, Phys. Rev. B **84**, 205327 (2011).

[81] I. Crassee, J. Levallois, A. L. Walter, M. Ostler, A. Bostwick, E. Rotenberg, T. Seyller, D. van der Marel, and A. B. Kuzmenko, Giant Faraday rotation in single- and multilayer graphene, Nat. Phys. **7**, 48 (2011); R. Shimano, G. Yumoto, J. Y. Yoo, R. Matsunaga, S. Tanabe, H. Hibino, T. Morimoto, and H. Aoki, Quantum Faraday and Kerr rotations in graphene, Nat. Commun. **4**, 1841 (2013).

[82] D. G. Dimitriu and D. O. Dorohoi, New method to determine the optical rotatory dispersion of inorganic crystals applied to some samples of Carpathian Quartz, Spectrochim. Acta Part A **131**, 674 (2014).

[83] L. A. Pajdzik and A. M. Glazer, Three-dimensional birefringence imaging with a microscope tilting-stage. I. Uniaxial crystals, J. Appl. Crystallogr. **39**, 326 (2006).

[84] X. Liu, J. Yang, Z. Geng, and H. Jia, Simultaneous measurement of optical rotation dispersion and absorption spectra for chiral substances, Chirality **8**, 1071 (2022).

[85] J.-M. Poumirol, P. Q. Liu, T. M. Slipchenko, A. Y. Nikitin, L. Martin-Morento, J. Faist, and A. B. Kuzmenko, Electrically controlled terahertz magneto-optical phenomena in continuous and patterned graphene, Nat. Commun. **8**, 14626 (2017).

[86] I. Tutunnikov, U. Steinitz, E. Gershnabel, J-M. Hartmann, A. A. Milner, V. Milner, and I. Sh. Averbukh, Rotation of the polarization of light as a tool for investigating the collisional transfer of angular momentum from rotating molecules to macroscopic gas flows, Phys. Rev. Res. **4**, 013212 (2022); U. Steinitz and I. Sh. Averbukh, Giant polarization drag in a gas of molecular super-rotors, Phys. Rev. A **101**, 021404(R) (2020).

[87] L. Tschugaeff, Anomalous rotatory dispersion, Trans. Faraday Soc. **10**, 70 (1914).

[88] R. E. Newnham, *Properties of Materials—Anisotropy, Symmetry, Structure* (Oxford University Press, New York, 2005).

[89] N. Tischler, M. Krenn, R. Fickler, X. Vidal, A. Zeilinger, and G. Molina-Terriza, Quantum optical rotatory dispersion, Sci. Adv. **2**, e1601306 (2016).

[90] J. H. Woo, B. K. M. Gwon, J. H. Lee, D-W. Kim, W. Jo, D. H. Kim, and J. W. Wu, Time-resolved pump-probe measurement of optical rotatory dispersion in chiral metamaterial, Adv. Opt. Mater. **5**, 1700141 (2017).

[91] Q. Zhang, E. Plum, J-Y. Ou, H. Pi, J. Li, K. F. MacDonald, and N. I. Zheludev, Electrogyration in metamaterials: Chirality and polarization rotatory power that depend on applied electric field, Adv. Opt. Mater. **9**, 2001826 (2021).

[92] J. Mun, M. Kim, Y. Yang, T. Badloe, J. Ni, Y. Chen, C.-W. Qiu, and J. Rho, Electromagnetic chirality: From

fundamentals to nontraditional chiroptical phenomena., Light Sci. Appl. **9**, 139 (2020).
[93] J. Ma and D. A. Pesin, Dynamic Chiral Magnetic Effect and Faraday Rotation in Macroscopically Disordered Helical Metals, Phys. Rev. Lett. **118**, 107401 (2017).
[94] U. Dey, S. Nandy, and A. Taraphder, Dynamic chiral magnetic effect and anisotropic natural optical activity of tilted Weyl semimetals, Sci. Rep. **10**, 2699 (2020).
[95] R. Gueroult, Y. Shi, J-M. Rax, and N. J. Fisch, Determining the rotation direction in pulsars, Nat. Commun. **10**, 3232 (2019).
[96] R. Gueroult, J.-M. Rax, and N. J. Fisch, Enhanced tuneable rotatory power in a rotating plasma, Phys. Rev. E **102**, 051202(R) (2020).
[97] P. D. S.Silva and M. M. Ferreira Jr., Rotatory power reversal induced by magnetic current in bi-isotropic media, Phys. Rev. B **106**, 144430 (2022).
[98] P. Hosur and X-L. Qi, Tunable circular dichroism due to the chiral anomaly in Weyl semimetals, Phys. Rev. B **91**, 081106(R) (2015).
[99] M. Nieto-Vesperinas, Optical theorem for the conservation of electromagnetic helicity: Significance for molecular energy transfer and enantiomeric discrimination by circular dichroism, Phys. Rev. A **92**, 023813 (2015).
[100] Y. Tang and A. E. Cohen, Enhanced enantioselectivity in excitation of chiral molecules by superchiral light, Science **332**, 333 (2011).
[101] M. Amin, O. Siddiqui, and M. Farhat, Linear and Circular Dichroism in Graphene-Based Reflectors for Polarization Control, Phys. Rev. Appl. **13**, 024046 (2020).
[102] V. G. Veselago, The electrodynamics of substances with simultaneously negative values of ϵ and μ, Sov. Phys. Usp. **10**, 509 (1968).
[103] D. R. Smith, W. J. Padilla, D. C. vier, S. C. Nemat-Nasser, and S. Schultz, Composite Medium with Simultaneously Negative Permeability and Permittivity, Phys. Rev. Lett. **84**, 4184 (2000).
[104] R. A. Shelby, D. R. Smith, and S. Schultz, Experimental verification of a negative index of refraction, Science **292**, 77 (2001).
[105] C. G. Parazzoli, R. B. Greegor, K. Li, B. E. C. Koltenbah, and M. Tanielian, Experimental Verification and Simulation of Negative Index of Refraction using Snells' Law, Phys. Rev. Lett. **90**, 107401 (2003).
[106] A. A. Houck, J. B. Brock, and I. L. Chuang, Experimental Observations of a Left-Handed Material that Obeys Snell's Law, Phys. Rev. Lett. **90**, 137401 (2003).
[107] M. Kadic, G. W. Milton, M. van Hecke, and M. Wegener, 3D metamaterials, Nat. Rev. Phys. **1**, 198 (2019).
[108] *Metamaterials: Physics and Engineering Explorations*, edited by N. Engheta and R. W. Ziolkowski (Wiley-Interscience, New Jersey, 2006).
[109] J. Liu, M. J. Luo, Q. Wang, and H.-J. Xu, Refractive index of light in the quark-gluon plasma with the hard-thermal-loop perturbation theory, Phys. Rev. D **84**, 125027 (2011).
[110] M. Y. Jamal, S. Mitra, and V. Chandra, Optical properties of an anisotropic hot QCD medium, J. Phys. G **47**, 035107 (2020).
[111] C.-W. Qiu, H.-Y. Yao, L.-W. Li, S. Zouhdi, and T.-S. Yeo, Routes to left-handed materials by magnetoelectric couplings, Phys. Rev. B **75**, 245214 (2007).
[112] L. Zhang, T. Koschny, and C. M. Soukoulis, Creating double negative index materials using the Babinet principle with one metasurface, Phys. Rev. B **87**, 045101 (2013).
[113] S. Zhang, Y.-S. Park, J. Li, X. Lu, W. Zhang, and X. Zhang, Negative Refractive Index in Chiral Metamaterials, Phys. Rev. Lett. **102**, 023901 (2009).
[114] J. Zhou, J. Dong, B. Wang, T. Koschny, M. Kafesaki, and C. M. Soukoulis, Negative refractive index due to chirality, Phys. Rev. D **79**, 121104 (2009).
[115] C.-Y. Chen, M.-C. Hsu, C. D. Hu, and Y. c. Lin, Natural Negative-Refractive-Index Materials, Phys. Rev. Lett. **127**, 237401 (2021).
[116] P. Ball, Bending the rules, naturally, Nat. Mater. **21**, 2 (2022).
[117] B. Guo, Chirality-induced negative refraction in magnetized plasma, Phys. Plasmas **20**, 093596 (2013).
[118] M. X. Gao, B. Guo, L. Peng, and X. Cai, Dispersion relations for electromagnetic wave propagation in chiral plasmas, Phys. Plasmas **21**, 114501 (2014).
[119] O. Sakai and K. Tachibana, Plasmas as metamaterials: A review, Plasma Sources Sci. Technol. **21**, 013001 (2012).
[120] O. Sakai, A. Iwai, Y. Omura, S. Lio, and T. Naito, Wave propagation in and around negative-dielectric-constant discharge plasma, Phys. Plasmas **25**, 03191 (2018).
[121] R. Gueroult, J.-M. Rax, and N. J. Fisch, Wave propagation in rotating magnetised plasmas, Plasma Phys. Controlled Fusion **65**, 034006 (2023).
[122] E. J. Post, *Formal Structure of Electromagnetics: General Covariance and Electromagnetics* (Norht-Holland Publishing Company, Amsterdam, Dover Publications, 1997).
[123] E. V. Gorbar, V. A. Miransky, I. A. Shovkovy, and P. O. Sukhachov, Chiral magnetic plasmons in anomalous relativistic matter, Phys. Rev. B **95**, 115202 (2017).
[124] E. V. Gorbar, V. A. Miransky, I. A. Shovkovy, and P. O. Sukhachov, Chiral magnetic plasmons in anomalous relativistic matter, Phys. Rev. B **95**, 115422 (2017).
[125] P. Sikivie, Invisible axion search methods, Rev. Mod. Phys. **93**, 015004 (2021).
[126] A. J. Millar G. G. Raffelt, J. Redondo, and F. D. Steffen, Dielectric haloscopes to search for axion dark matter: Theoretical foundations, J. Cosmol. Astropart. Phys. 01 (2017) 061.
[127] M. Lawson, A. J. Millar, M. Pancaldi, E. Vitagliano, and F. Wilczek, Tunable Axion Plasma Haloscopes, Phys. Rev. Lett. **123**, 141802 (2019).
[128] A. J. Millar *et al.*, Searching for dark matter with plasma haloscopes, Phys. Rev. D **107**, 055013 (2023).